Fall 12-20-2012

Multiband Detectors and Application of Nanostructured Anti-Reflection Coatings for Improved Efficiency

J. A. Ranga C. Jayasinghe

MULTIBAND DETECTORS AND APPLICATION OF NANOSTRUCTURED ANTI-REFLECTION COATINGS FOR IMPROVED EFFICIENCY

by

J. A. RANGA CHAMINDA JAYASINGHE

Under the Direction of A. G. Unil Perera

ABSTRACT

This work describes multiband photon detection techniques based on novel semiconductor device concepts and detector designs with simultaneous detection of different wavelength radiation such as UV and IR. One aim of this investigation is to examine UV and IR detection concepts with a view to resolve some of the issues of existing IR detectors such as high dark current, non uniformity, and low operating temperature and to avoid having additional optical components such as filters in multiband detection. Structures were fabri-

cated to demonstrate the UV and IR detection concepts and determine detector parameters: (i) UV/IR detection based on GaN/AlGaN heterostructures, (ii) Optical characterization of p-type InP thin films were carried out with the idea of developing InP based detectors, (iii) Intervalence band transitions in InGaAsP/InP heterojunction interfacial workfunction internal photoemission (HEIWIP) detectors. Device concepts, detector structures, and experimental results are discussed. In order to reduce reflection, TiO_2 and SiO_2 nanostructured thin film characterization and application of these as anti-reflection coatings on above mentioned detectors is also discussed.

INDEX WORDS: Infrared detectors, UV/IR Dual-band detectors, Split-off band, GaAs, AlGaAs, GaN, AlGaN, InP, InGaAsP, TiO_2 nanorods, Anti-reflection coatings

MULTIBAND DETECTORS AND APPLICATION OF NANOSTRUCTURED ANTI-REFLECTION COATINGS FOR IMPROVED EFFICIENCY

by

J. A. RANGA CHAMINDA JAYASINGHE

A Dissertation Submitted in Partial Fulfillment of the Requirements for the Degree of

Doctor of Philosophy

in the College of Arts and Sciences

Georgia State University

2012

MULTIBAND DETECTORS AND APPLICATION OF NANOSTRUCTURED ANTI-REFLECTION COATINGS FOR IMPROVED EFFICIENCY

by

J. A. RANGA CHAMINDA JAYASINGHE

Committee Chair: Dr. A. G. Unil Perera

Committee: Dr. Brian D. Thoms

Dr. Vadym M. Apalkov

Dr. Douglas R. Gies

Dr. Alexander Y. Kozhanov

Electronic Version Approved:

Office of Graduate Studies

College of Arts and Sciences

Georgia State University

December 2012

DEDICATION

This dissertation is dedicated to my parents, my wife Ayesha, and my daughter Thenulya.

ACKNOWLEDGEMENTS

This dissertation work would not have been possible without the support of many people. I would like to express my deepest sense of gratitude to my advisor Dr. Unil Perera for his patient guidance, encouragement and excellent advice throughout this study. His constant enthusiasm, support, and invaluable suggestions made this work successful. Deepest gratitude is also due to the members of the supervisory committee: Dr. Brian Thoms, Dr. Vadym Apalkov, Dr. Douglas Gies, and Dr. Alexander Kozhanov for fruitful discussions, technical assistance, and effort in reading and providing me with valuable comments on this dissertation. I would like to convey special acknowledgment to Dr. Steven Matsik, Dr. Nikolaus Dietz, and Dr. Yang-feng Lao, who were always open for questions and discussions relating to my research and for their valuable scientific advice. Special thanks to former members Dr. Gamini Ariayawansa, Dr. Viraj Jayaweera, Dr. Mohamed Rinzan, Dr. Aruna Weerasekara, Mr. Greggory Rothmeier and Ms. Laura Byrum Patel for valuable discussions on the subject matters. I would also like to thank present colleagues in the group: Duleepa Pitigala, Yigit Aytac, Justin McLaughlin, Hiren Patel, and Dr. Jitto Titus. I am grateful to the collaborators with our research group, Dr. H. C. Liu, Dr. Mattias Hammar and Dr. Yipping Zhao for providing us with research samples. I wish to thank all the individuals of the Department of Physics and Astronomy, especially the Physics workshop team headed by Mr. Charles Hopper and Peter Walker who converted my mechanical drawings into physical reality, and friends for their contribution, friendship, love, and help. Finally, I take this opportunity to express my profound gratitude to my beloved parents, parents in law, and my wife for their moral support and patience during my study at GSU.

TABLE OF CONTENTS

LIST OF TABLES

LIST OF FIGURES

LIST OF ABBREVIATIONS

- AR - Antireflection
- AlGaAs - Aluminum Gallium Arsenide
- AlGaN - Aluminum Gallium Nitride
- CB - Conduction band
- D^* - Detectivity
- DF - Dielectric function
- eV - Electron volts
- FC - Free carrier
- FIR - Far-infrared
- FP - Fabry-Perot
- FTIR - Fourier Transform Infrared
- GaAs - Gallium Arsenide
- GaN - Gallium Nitride
- HEIWIP - Heterojunction interfacial workfunction internal photoemission
- *hh* - Heavy hole
- HIWIP - Homojunction interfacial workfunction internal photoemission
- InGaAsP - Indium Gallium Arsenide Phosphide
- InP - Indium Phosphide

- IR - Infrared
- IVB - Intervalence band
- *lh* - Light hole
- MIR - Mid-infrared
- NIR - Near-infrared
- PL - Photoluminescence
- TiO_2 - Titanium dioxide
- SiO_2 - Silicon dioxide
- *so* - Split-off
- UV - Ultraviolet
- VB - Valence band
- VIS - Visible

CHAPTER 1

INTRODUCTION

Multi-band detector technology is used in a number of exciting applications, such as military, medical imaging, remote sensing, fire/flame detection, and space situational awareness. Development and improvement of such technology in the Ultraviolet (UV) to infrared (IR) region is important and remains one of the critical aspects of the successful development of active and passive remote sensing abilities. Recent developments in UV and IR detector technology mainly involve device physics, semiconductor material growth and electrical/optical characterization techniques. Typically, measuring multiple wavelength bands requires either multiple detectors or a single broad-band detector coupled to a filter wheel which is used to filter out unwanted incident light from different wavelength regions. These type of systems require complex detector assemblies, separate cooling systems, additional electronic components, and extra optical elements (lenses, prisms, gratings, and beam splitters, etc.). In addition, these detector systems involve fine optical alignments which lead to sophisticated control hardware. Ultimately, these complications increase the weight and cost of the detector system. In fact, a single detector responding to both UV and IR bands will be a better solution which allows critical measurements at improved accuracy with a great reduction in system complexity, weight, and cost. For an instance, a single UV/IR dual-band detector reduces the burden of mounting two separate detectors and makes the process of mounting the detector on a fire fighter's helmet feasible due to its light weight. Furthermore, the UV/IR dual-band photodetectors also have potential applications in various areas, such as fire/flame detection,[5] solar astronomy, space situational awareness,[6] analysis of muzzle flashes from firearms,[7] and combustion process monitoring.[8, 9] For example, current missile-warning sensors are built to detect UV and IR radiation emitted by missile's plume. Therefore, in aforementioned missile-warning sensors, an UV/IR detector system should

be able to distinguish the missile plume against its complex background, avoiding possible false-alarms. Interestingly, these single element multi-band detectors consist of stacked arrangement of different materials in which the shorter wavelength detector is placed on top of the longer wavelength detector. Moreover, the top detector material absorbs only the shorter wavelength radiation and transmits the longer wavelength radiation to the bottom detector.

Group III-V compound semiconductor materials such as Gallium Arsenide (GaAs), Indium Arsenide (InAs), Gallium Nitride (GaN), and Indium Phosphide (InP) are popular semiconductors in current semiconductor research. These semiconductors and their alloys possess a range of properties that will be suitable for a vast number of applications such as photodetectors ranging from UV to far-infrared (FIR) range, light emitting diodes (LEDs) with different colors, lasers, bipolar transistors, and electro-optic modulators. Therefore, the characterization of these materials is very important. Among these characterization techniques, optical characterization techniques such as IR reflectance/transmittance spectroscopy, Raman spectroscopy, and photoluminescence spectroscopy are popular due to their ability for non-destructive material testing. In fact, IR reflectance/transmittance spectroscopy is used to investigate the IR dielectric function of these materials which is an important parameter for designing optoelectronic devices. The IR dielectric function includes both free carrier absorption and intervalence band (IVB) absorption. The IVB absorption is due to hole transitions between lh, hh, and so bands. The well-known Drude model is used for free carrier absorption and Lorentzian oscillator model for phonon absorption in the lattice and a recently developed mathematical model [10] is used for IVB absorption. The IR dielectric function is used to extract mainly the absorption coefficient and refractive index of the medium. In addition, either effective mass or carrier concentration can be evaluated if one parameter is known explicitly.

Among different types of IR detectors, Interfacial Workfunction Internal Photoemission (IWIP) detectors have the advantage being fast compared to the thermal detectors. These IWIP detectors can be categorized as either Homojunction (HIWIP)[11, 12] or HEterojunc-

tion (HEIWIP)[13, 14] detectors. Furthermore, both types of detectors consist of a series of doped emitters and undoped barriers with detection by a three stage process: (i) free carrier absorption, (ii) internal photoemission, and (iii) collection of emitted carriers. The band diagram for a single GaN/AlGaN emitter-barrier period[15] as shown in Fig. 1.1. These detectors use intraband transitions in the emitter to provide the IR response. However, the limit on the response wavelength is introduced in the photoemission stage. Moreover, carriers will be trapped in the emitter unless they have sufficient energy to pass over the barrier. This introduces a work function Δ, corresponding to the energy difference between the top of the barrier and the Fermi energy in the emitter. The threshold wavelength, λ_0 (in μm) is determined as $\lambda_0 = 1240/\Delta$ with Δ in meV. Once the carriers have undergone internal photoemission, they are then swept out of the device by the external electric field and are collected at the contact. Furthermore, the fundamental difference between the HIWIP and HEIWIP detectors is that HIWIP detectors use the same bandgap material for barriers and emitters, while HEIWIP detectors use different bandgap materials for the emitters and barriers. Therefore, for HIWIPs, the barrier is due to the bandgap offset from the doping Δ_d, i.e., $\Delta = \Delta_d$, while for HEIWIPs, there will be an additional contribution Δ_x from the bandgap offset due to the Al fraction difference, and $\Delta = \Delta_d + \Delta_x$. The contribution from the doping Δ_d is found as in Ref. [11], giving a value near zero for n-GaN in the range 10^{17} - 10^{19} cm^{-3}. The Al fraction contribution is taken as $\Delta_x = 2000\Delta$x meV where Δ_x is the difference in the Al fraction (x) between the emitter and barrier layers. Aside from the difference in Δ, the response calculations for the two types of detectors are identical. A fully detailed IR detector design is reported in Ref. [16].

There is a significant reflection at the top surface of a photodetector due to the abrupt change in refractive index from air to semiconductor surface. For instance, there is more than 30 % reflection from an air-GaN interface in near- to mid-IR wavelengths. This reflection can be minimized by implementing a multi-layer anti-reflection (AR) coating having a gradient refractive index profile. Graded refractive index profile will reduce the reflection at each interface for adjacent layers in the multi-layer stack due to gradual change of refractive

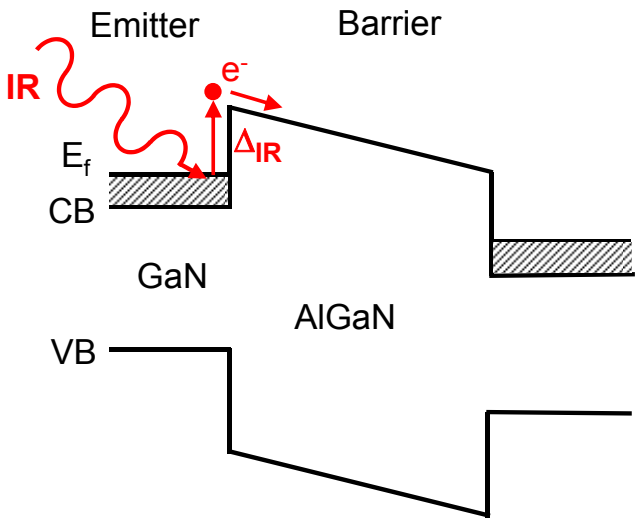

Figure 1.1 Detector structure of a single period GaN/AlGaN heterojunction detector. The top and bottom layers are highly n-doped. Top contact serves as an emitter and the middle layer as a barrier.

index from semiconductor surface to the air medium. Hence, it will drastically reduce the total reflection. Therefore, the detector will have broad spectral range and wide angle of view. In these multi-layer AR coatings having graded refractive index, the layers closer to the air interface should have very low refractive index. This is possible due to recently developed SiO_2 and TiO_2 nanorod layers. These nanorods are grown using an oblique angle deposition technique, and due to the porosity of the structure the nanostrucuted layer has very low refractive index. The refractive index of the layer can be changed by varying the flux angle of the vapor used in growth. The lowest refractive index reported so far is 1.05 with SiO_2 nanorods.[17] Therefore, it is important to study the optical characterization of nanorods in order to better design aforementioned multi-layer AR coatings. Thus, these AR coatings can also be applied to solar cells to improve their efficiency and avoid sun tracking mechanisms.

In this dissertation, I present a study of electrical and optical characterization of group III-V heterostructures such as GaN/AlGaN and InGaAsP/InP. The GaN based material systems have attracted the interest of the scientific community for the development of wide bandgap optoelectronic devices. Among the different types of UV/IR detectors, GaN based detectors possess a significant role due to its visible blind characteristics. Therefore these detectors do not respond to visible light, and thus the false detection rate is strongly reduced. Furthermore, in Chapter 2, the results introduce a novel GaN/AlGaN single element detector, which is capable of identifying both the UV (250 - 360 nm) and IR (5 - 14 μm) responses with near zero spectral cross talk, separately but in a simultaneous manner. The detector consists of two distinct active regions for UV and IR detection, with separate electrical contacts. This has lead this detector to acquire a unique feature, where the UV response is based on interband transitions in the undoped barrier layer, while the IR response is from a HEIWIP structure. Moreover, it has also allowed the thresholds of the UV and IR responses to be tailored by adjusting the Al fraction.

Semiconductor materials should be explored and investigated in order to improve the opto-electronic devices. In Chapter 3, p-InP thin films with different doping values have

been investigated using IR reflectance and transmittance spectroscopy. The IR dielectric function obtained from absorption curve fitting is used to extract the absorption coefficient and refractive index of the thin films. Both IVB absorption and free carrier absorption are used to extract the total absorption coefficient. In addition, the effective mass of holes is evaluated in cryogenic temperatures, which is not yet reported from experimental measurements in the literature. This study will also be beneficial to IR detector designing and study the additional loss in phosphide based lasers due to IVB absorption.

Even though InGaAsP/InP material system has been widely used in Quantum Well Infrared Photodetectors (QWIPs)[18] and laser [19] structures, the IVB absorption in this material system is not well studied. IR detectors in 3 - 5 μm range, based on IVB hole transitions have been recently reported [20] using p-GaAs/AlGaAs heterostructures. Moreover, high operating temperatures and additional absorption on top of free carrier absorption of these devices attracted the applications in the civilian, industrial, medical, astronomy and military sectors. However, the spectral range of these detectors can be extended in to mid-infrared (MIR) region by varying the materials with different *so* splitting energies (Δ_{so}). For an instance, InP will allow 2 - 10 μm detection (Δ_{so}(InP) = 0.108 eV). In Chapter 4, an InGaAsP/InP HEIWIP detector is used to demonstrate IR response originating from hole transitions between lh/hh bands and the *so* band. Interestingly, this detector has p-type InGaAsP as emitters and undoped InP as barriers and works in the mid IR region. Furthermore, this detector was designed to operate in mid-IR region which has free carrier threshold wavelength of 10 μm and split-off threshold of 6.8 μm. Importantly, the significance of having InGaAsP as the emitter material is that the ability to tune the split-off threshold from 3.3 - 11 μm by varying the As fraction. Due to these properties and effects this device is used to study the temperature dependence of IVB transitions in InGaAsP.

In Chapter 5, a detail description of an analysis of nanostructured AR coatings and its applications have been discussed. Interestingly, in nanostructured AR coatings, the property of graded refractive index allows improved light transmission (due to the effect of drastic reduction of reflected light) into detector even at high angle of incidence over a broad spec-

tral range. This will enhance the performance of the detection over a wide spectral response region. Theoretically, the total reflection will be near zero if number of layers in the AR coating is infinite. However, having a large number of layers is not feasible in practical situations due to growth issues and cost. Furthermore, in Chapter 5, designing and optimizing of such AR coatings with less number of layers is discussed. Feasibility of TiO_2 nanorods on these AR coatings to achieve low refractive index is also discussed. Therefore, single layer TiO_2 nanorods grown on either glass or Si substrate are optically characterized in visible and IR regions.

CHAPTER 2

SIMULTANEOUS DETECTION OF ULTRAVIOLET AND INFRARED RADIATION IN A SINGLE GaN/AlGaN HETEROJUNCTION

2.1 Introduction

Presently, as a group III-V material, GaN has attracted the interest of the scientific community for the development of wide bandgap electronic and optoelectronic devices. The GaN/AlGaN material systems can be used to further improve multi-band photodetectors which have advantages in different wavelength regions compared to the GaAs/AlGaAs system.[21–23] Dual-band detectors operating in the near-, mid-, and far-infrared regions based on the group III-As material[24–27] systems have been previously reported. Ultraviolet (UV) detectors,[8, 9] UV light emitting diodes,[28, 29] and UV laser diodes[30] have been successfully demonstrated. UV/IR dual-band photodetectors have potential applications in various areas, such as fire/flame detection,[5] solar astronomy, military sensing, situational awareness applications, and combustion process monitoring.[8, 9] Since the UV/IR dual-band detectors do not respond to visible light, the false detection rate is strongly reduced. In the far-IR region, GaN-based detectors can be used to access the reststrahlen region of GaAs gaining a broad response from 20 μm and beyond. The radiation hardness of GaN due to its wide bandgap is another advantage over GaAs. This will also reduce interband tunneling compared to the case of GaAs based devices. Moreover, the higher effective electron mass for GaN will reduce the thermal emission. However, the growth of high-quality GaN/AlGaN heterostructures is limited by the lack of knowledge on growth processes and availability of suitable lattice-matched substrate materials. In this chapter, I present a study of a HeterojunctionInterfacial Workfunction Internal Photoemission (HEIWIP) detector[31] based on GaN/AlGaN heterostructures, which can simultaneously detect both UV and IR radiation with minimal spectral cross talk.

UV/IR dual-band detectors are particularly useful in applications where the detection of both the UV and IR radiation is important. One example is fire and flame detection where fires emit radiation from the UV to the IR, and different flames such as hydrogen and coal have significant intensity variations in their emission spectrum in the UV and IR regions. A two terminal detector responding in both the UV and mid-IR range (where both photo current components were collected from the same two terminals) was reported previously.[15] This limits the usefulness of the device, since it could not easily identify whether only the UV or IR radiation or a combination is detected.

2.2 UV/IR Detection Mechanisms

A typical single emitter/barrier period GaN/AlGaN UV/IR two terminal detector[15] is shown Fig. 2.1(a). The detection mechanism is shown in Fig. 2.1(b) along with the energy band diagram. These detectors use intraband transitions in the emitter to provide the IR response. For IR, the limit on response wavelength is introduced in the photoemission stage. Carriers will be trapped in the emitter unless they have sufficient energy to pass over the barrier. This introduces a workfunction Δ_{IR}, corresponding to the energy difference between the top of the barrier and the Fermi energy in the emitter. The threshold wavelength, λ_{IR} (in μm) is determined as $\lambda_{IR} = 1240/\Delta_{IR}$ with Δ_{IR} in meV. Once the carriers have undergone internal photoemission, they are then swept out of the device by the external electric field and are collected at the contact. This Δ_{IR} is mainly due to the bandgap offset between GaN and AlGaN layers. There will be an additional contribution from doping is found as in Ref. [11] near zero for n-GaN in the range 10^{17} - 10^{19} cm^{-3}. A fully detailed IR detector design is reported in Ref. [16].

HEIWIP UV/IR dual-band detector structures with n-doped GaN emitters and undoped AlGaN barriers are presented. There are two detection mechanisms leading to dual-band response: (i) interband (valence-to-conduction) transitions of carriers in the undoped barrier leading to UV response, and (ii) intraband transitions in the doped emitter resulting in a response in mid-infrared (MIR) to far-IR (FIR) region. The wavelength threshold of the

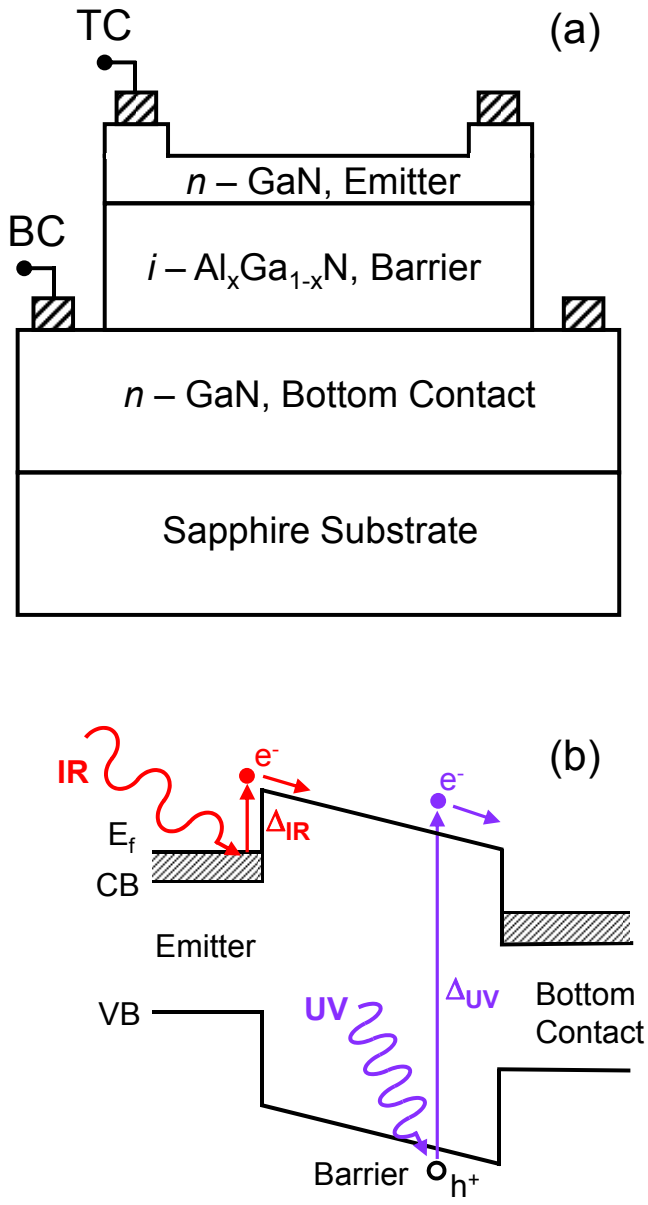

Figure 2.1 (a) Schematic diagram of a typical GaN/AlGaN HEIWIP structure having only two output terminals (top and bottom metal contacts). The doping concentration of the GaN emitter and bottom contact is 5×10^{18} cm^{-3}. The AlGaN barrier is not doped. (b) The corresponding band diagram showing the conduction/valence band (CB/VB) profile of the structure and the transitions leading to UV/IR dual-band responses.

interband response depends on the band gap of the barrier material, and the MIR/FIR response depends on intraband transitions in the emitter.

2.2.1 GaN UV Detector Background

The UV absorption takes place in the barrier region of the device. Due to autodoping in GaN, it is expected that the barrier region will actually be n-doped to 10^{17} cm^{-3} due to unintentional doping. This autodoping may enhance the UV detection by increasing the gain in the UV detector due to trapping of minority carriers at the interface.[32] The bandgap between the valence and conduction bands in $Al_xGa_{1-x}N$ is given by

$$E_g = 6.13x + 3.42(1-x) - 1.08x(1-x)eV. \tag{2.1}$$

The UV threshold wavelength λ_{og} (in nm) is then given by $\lambda_{og} = 1240/E_g$ where E_g is measured in eV. The device operates similarly to the UV detectors previously demonstrated on GaN.[33, 34] The width of the depletion region formed in the barrier will change with the applied bias. The interband absorption will then excite electrons from the valence to the conduction band producing an electron-hole pair. These electrons will be swept out of the barrier region by the electric field and will be collected at the contact. This type of UV detector has shown a very high gain of 1000 or more.[32, 35] This gain has been explained in terms of a barrier lowering in a Schottky contact. The basic idea of the gain in a Schottky detector is that the minority carriers (in this case, holes) are trapped at the metal-semiconductor interface. The resulting charge produces a lowering of the Schottky barrier, leading to an enhanced photocurrent.

2.3 Experiment

The dual-band detector design (see Fig. 2.2(a)) reported here has separate UV- and IR-active regions with three contacts (one common contact for both regions) to measure separately the UV and IR photocurrent components simultaneously. The structure consists

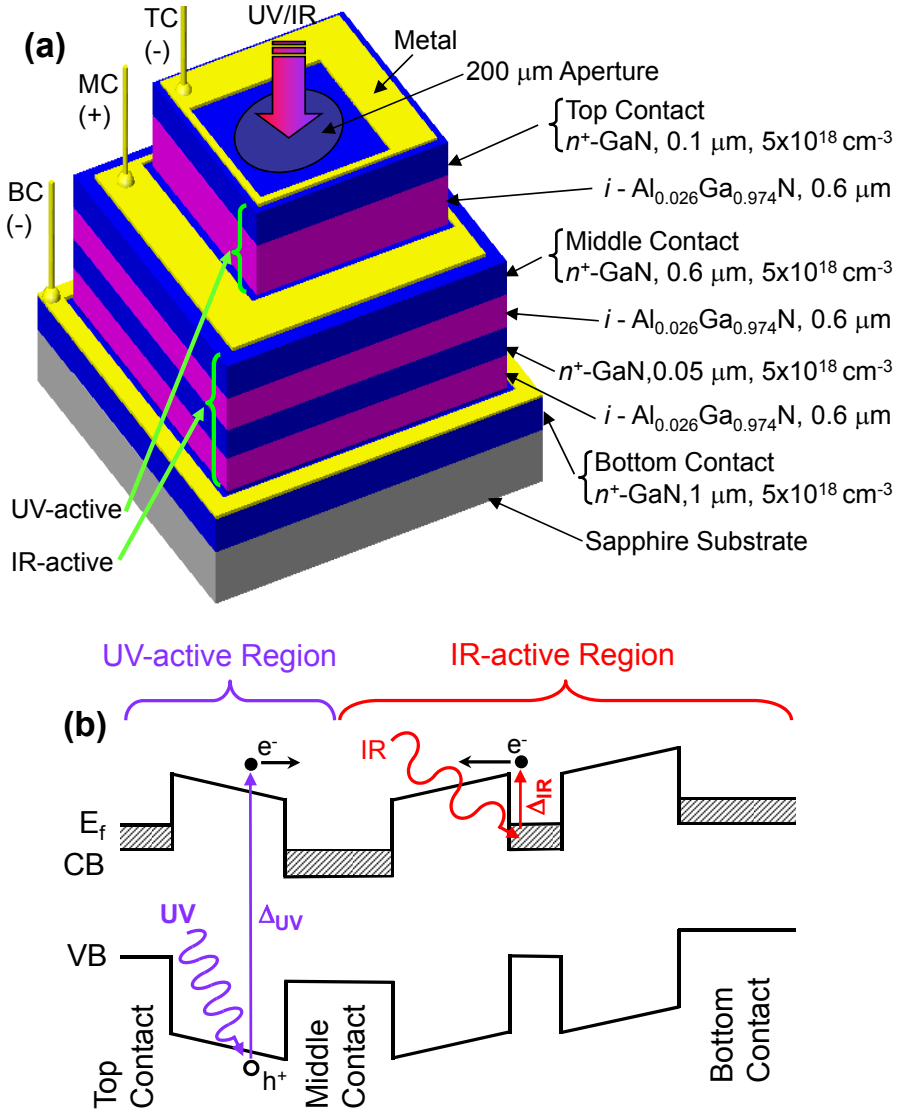

Figure 2.2 The three contact structure for simultaneous dual-band response measurements showing, (a) Separate active regions for UV and IR measurements and (b) the corresponding band diagram (CB and VB are the conduction and valance bands, respectively) under reverse bias configuration. Three contacts allow separate readouts from the UV- and IR-active regions. The labels TC, MC, and BC indicate the top-, middle-, and bottom-contacts, respectively, and (+) or (-) shows the relative potential at which the device was operated. A 200 μm aperture was used to block the radiation leakage through the outer openings to the IR-active region.

of an n^+-GaN top-contact (TC) layer, a UV-active region of an undoped $Ga_{0.974}Al_{0.026}N$ layer, an n^+-GaN middle-contact (MC) layer, an IR-active region, and a bottom-contact (BC) layer. The IR-active region consists of two periods of an n^+-GaN emitter layer and an undoped $Ga_{0.974}Al_{0.026}N$ barrier layer, and either the MC or BC acts as an emitter depending on the bias. The AlGaN epitaxial layers were grown by low pressure metal-organic chemical vapor deposition (MOCVD) on c-plane sapphire substrates, and the devices structures were processed by dry etching, and contacts were made by depositing Ti/Al/Ti/Au [30/80/120/55 nm]. A ring contact was used on the top surface and a window was opened through the top contact for front side illumination. The electrical area of the device is 400×400 μm^2 and the optical area is 270×270 μm^2.

The UV response is due to interband absorption in the top $Ga_{0.974}Al_{0.026}N$ layer producing electron-hole pairs, which are then swept out by an external electric field, and collected at the contacts. The UV response threshold is given by the Al fraction in the $Ga_{0.974}Al_{0.026}N$ layer. The offset between the Fermi level in the emitter layer and the conduction band edge of the barrier layer forms the interfacial work function Δ, which arises due to the band offset of different materials[16] and the band gap narrowing[36] of the n^+-GaN emitter layer. The IR response is due to free carrier absorption in the emitters and internal photoemission over the work function at the emitter barrier interface, followed by collection at the contacts using an external electric field. The thresholds for the UV and IR responses can be controlled separately by using AlGaN for both the emitter and barrier layers. Thus, by adjusting the Al fraction in the barrier (x), both the UV and IR thresholds will change and adjusting the Al fraction in the emitter (y) allows the IR threshold to be tailored without changing the UV threshold. Adjusting both x and y, the UV threshold can be changed without changing the IR threshold.

2.4 Results and Discussion

Throughout this discussion, the MC-terminal is the common terminal. Hence, forward (reverse) bias denotes that the TC-terminal for the UV-active region or the BC-terminal

for the IR-active region is positive (negative) relative to the MC-terminal. When the TC layer is negatively biased, it also acts as an emitter, making the IR detection possible in the UV-active region. This effect can be decreased by reducing the TC layer thickness, which reduces the IR absorption and the generated photocurrent. Furthermore, this TC layer absorbs UV radiation, suppressing the transmission of UV into the UV-active region, without generating photocurrent, because the excited electron-hole pairs are trapped by the barriers and recombine in the highly doped TC. For an optimum UV response, the TC layer thickness was found to be 0.1 μm, which is thin enough to reduce the IR absorption while still giving uniform electric field distribution across the UV-active region. Furthermore, the generation of IR photocurrent is prominent in the IR-active region, while no UV photocurrent is expected irrespective of the bias configuration, since almost all the UV radiation is absorbed within the UV-active region.

For simultaneous UV and IR photocurrent measurement with a near zero spectral crosstalk, the direction of the applied electric field across each region should be determined based on the following considerations. A UV photocurrent from the UV-active region is expected for both forward and reverse bias configurations, while an IR photocurrent from the UV-active region is not expected under reverse bias as explained before. From the IR-active region, an IR photocurrent is expected for both forward and reverse bias, while no UV photocurrent is expected under any bias configuration. Hence, simultaneous measurement of UV and IR generated photocurrent components with near zero spectral crosstalk is possible when the UV- and IR-active regions are under reverse bias configuration with the corresponding band diagram as shown in Fig. 2.2(b). Under this configuration, the majority carriers move toward the MC and would not move from one active region into the other.

For the simultaneous spectral measurements, a chopper (see Fig. 2.3) was used to modulate both the UV and IR radiations, providing the same modulation as in a typical application (see Appendix B for more details). The responses from both active regions were obtained simultaneously at 77 K as shown in Fig. 2.4. The UV spectra were obtained by using a Deuterium UV source, DK480 1/2 meter monochromator, and neutral density filters. The

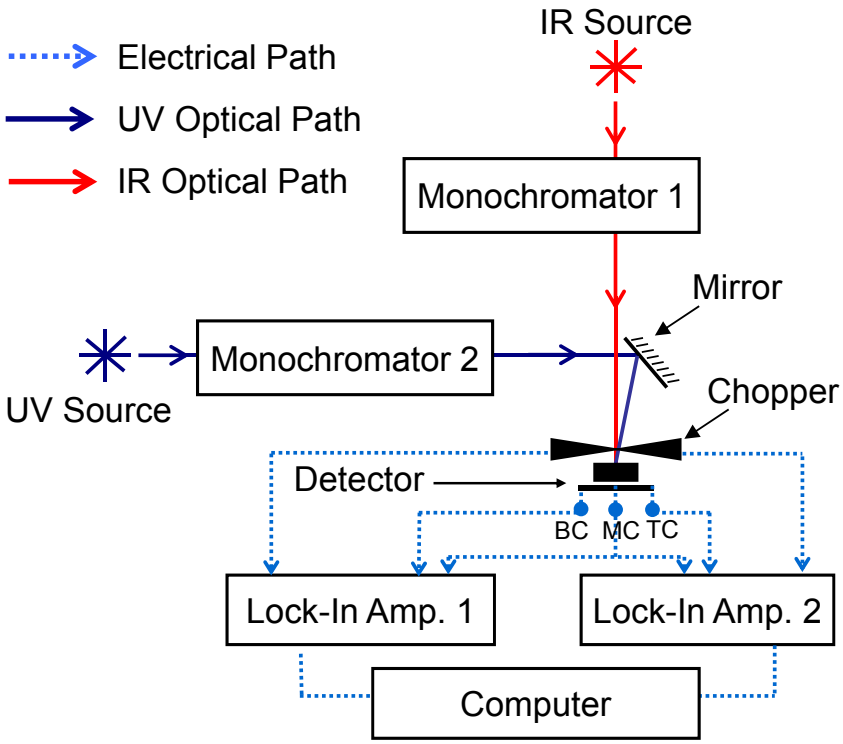

Figure 2.3 The experimental setup for measuring the UV and IR components simultaneously. A single optical chopper is used to modulate the incoming radiation, as in a typical application. The monochromators and lock-in-amplifiers are controlled by a computer to obtain both responsivities.

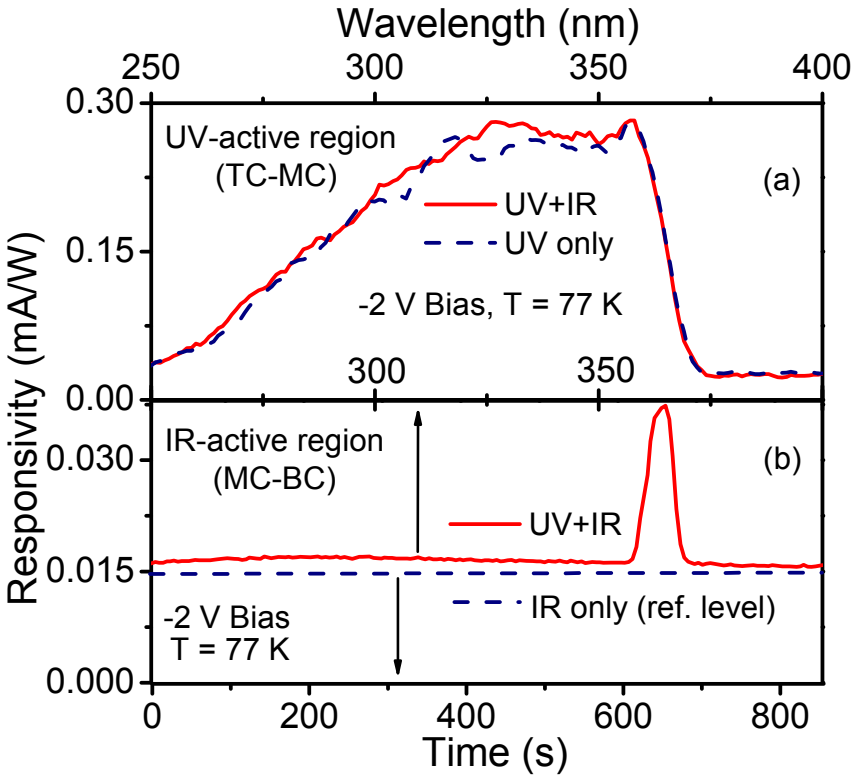

Figure 2.4 Simultaneously measured photo currents (solid lines) from (a) UV-active region (TC-MC) and (b) IR-active region (MC-BC) at 77 K, when both IR and UV radiation were incident onto the detector. The UV wavelength was varied between 250 - 400 nm, while IR was fixed at 9.3 μm (using a CO_2 laser). The dashed line in (a) represents the photocurrent when only UV radiation was incident and the dashed line in (b) indicates the response level (which is constant with time), as a reference level for the "UV+IR" response from the IR-active region, when only IR radiation was incident which only corresponds to the bottom axis. The lower and upper x-axes of (a) are also the upper axis of (b).

UV spectra were calibrated using a background spectrum obtained by a Hamamatsu photomultiplier tube with a known sensitivity. A CO_2 laser at 9.3 μm with 0.1 W output power was used as the IR source. The solid lines show simultaneously measured photocurrents from UV-active region (Fig. 2.4(a)) and IR-active region (Fig. 2.4(b)) at 77 K, when both IR and UV radiations were incident onto the detector. The UV wavelength was varied between 250 - 400 nm, while IR radiation was fixed at 9.3 μm (using a CO_2 laser). The dashed line in Fig. 2.4(a) represents the photocurrent when only the UV radiation was incident. The dashed line in Fig. 2.4(b) indicates the response level as a reference when only the IR radiation was incident. No significant change in response was observed due to IR radiation in the UV-active region. The change in response due to UV radiation from the IR-active region is almost zero except for the exciton peak observed around 365 nm. The upper and lower x-axes of Fig. 2.4(a) show the wavelength range 250-400 nm. The lower x-axis of Fig. 2.4(a) also serves as the upper x-axis of Fig. 2.4(b). The IR response shown in Fig. 2.4(b) does not correspond to the wavelength scale and only corresponds to the time scale of the bottom axis.

The broad IR responses from both active regions obtained separately at 77 K are shown in Fig. 2.5, with free carrier response seen as a broad peak with a maximum near 11 μm. The UV active region did not show a measurable IR response under negative bias, but did show a response under positive bias as expected. The broad IR spectra were calibrated using a background spectrum obtained with a Si composite bolometer with the same set of optical components.

A 200 μm diameter aperture (as shown in Fig. 2.2(a)) was used to block the UV radiation leakage (i.e., entering the IR-active region without passing through the UV-active region) through the region around the MC. This removed the UV response from the IR-active region except for the narrow response peak at 365 nm (Fig. 2.4(b)). This response peak can be due to one of two reasons. It could be due to a light transmission as a result of a generation-recombination mechanism of an exciton.[37] An exciton (365 nm) generated in the top AlGaN layer in the UV-active region could relax re-emitting a UV photon, which could generate

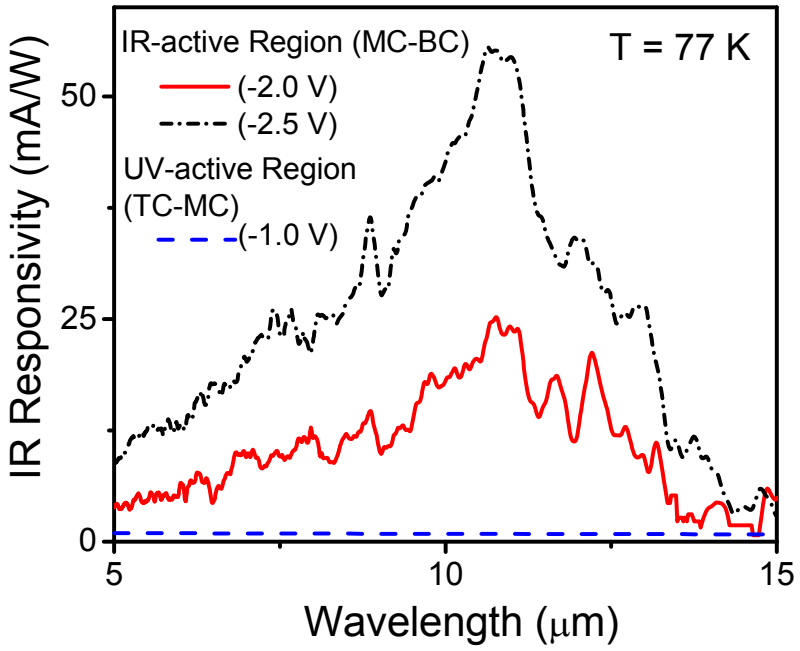

Figure 2.5 The IR response from IR- and UV-active regions at 77 K. The UV-active region showed almost zero response for IR radiation under reverse bias configuration as expected.

another exciton, and so on, allowing a small fraction of photons at 365 nm to pass through to the IR-active region. The second reason is that the low energy UV radiation which has an energy below the band gap of $Ga_{0.974}Al_{0.026}N$ was absorbed in the MC layer, and the generated photocurrent could be either due to the minority carrier transportation[38] in the structure where the generated holes were recombined with the electrons in the valance band, or electron hopping from the filled impurity acceptor levels above the valance band of AlGaN layers. However, further studies are needed to verify these ideas.

In an ideal dual-band detector, the UV response should be obtained solely from the UV-active region, and the IR response from the IR-active region. Tests were carried out varying the combination of incident radiation while keeping the UV wavelength fixed at 300 nm and IR wavelength fixed at 9.3 μm. The results are listed as voltage signals for fixed load resistor values as given in Table 2.1 showing no change in response for IR radiation in the UV-active region, and a near noise level change for UV radiation in the IR-active region (i.e., near zero spectral cross-talk). The voltage signal could be used to identify the response from each active region, and would only vary from the photocurrent signal by a constant factor.

The current vs. voltage curves for the detector under dark conditions is shown in Fig. 2.6 for 80 K and 300 K. There is significant asymmetry seen in the UV-active region for low temperature. This is due to the middle GaN contact layer being thicker than the top GaN contact layer. The dark current in the UV-active region is lower than that of IR-active region for low bias values and higher negative bias values. The extra dark current can be coming from the more emitters in the IR-active region. In fact, for simultaneous and separate detection of UV and IR photo currents, the top and bottom contacts are negatively biased while middle contact is positively biased. Therefore, under these bias conditions the device operates in the lowest dark current conditions.

Table 2.1 Response for Different Combinations of Incident Radiation[a]

UV-active region (TC-MC)

	With UV	Without UV
With IR	6.0 mV	0.0 mV
Without IR	6.0 mV	0.0 mV

IR-active region (MC-BC)

	With UV	Without UV
With IR	1.5 mV	1.4 mV
Without IR	0.1 mV	0.0 mV

[a]The wavelengths were held constant at 300 nm for UV and 9.3 μm for IR. The results were left as voltage signals for a fixed load resistor.

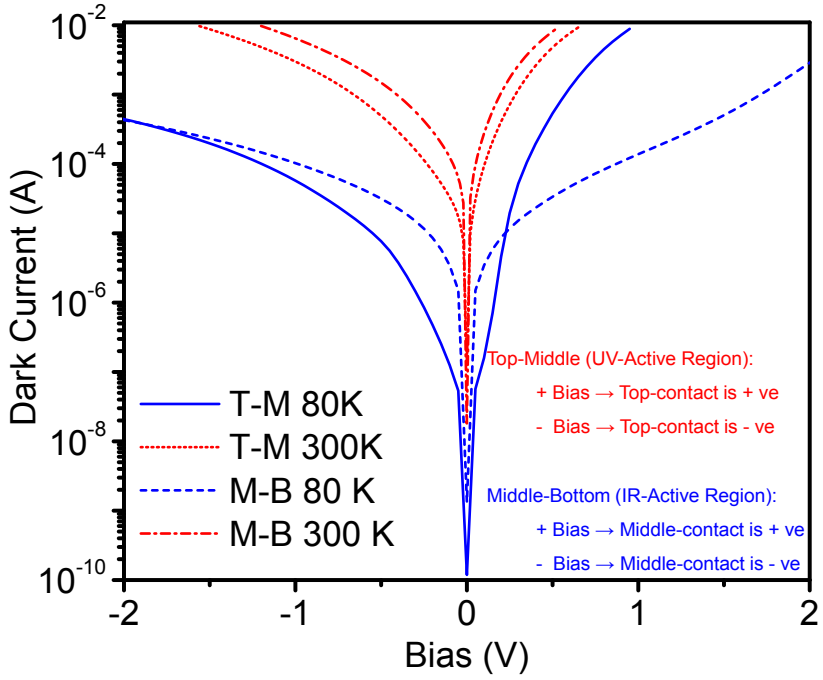

Figure 2.6 The I-V curves of the detector at 80 K and 300 K temperatures under dark conditions. T-M is the UV-active and M-B is the IR-active region. Here, T, M, and B denote top, middle, and bottom contacts, respectively. The polarity of the device for positive and negative bias is shown in the figure.

2.5 Improved Structures for Complete Blocking of UV Penetration

These detectors consist of a UV active region (between the top and middle contacts) with a 1.2 μm thick AlGaN layer and a single period IR active region (between the middle and bottom contacts). The structure is schematically shown in Fig. 2.7. Mesa detectors were formed by etching down to the bottom contact layer. An outer ring of the mesas was then etched down to the middle contact layer. Metal contacts, labeled as TMC, MMC, and BMC, were then deposited on the top, middle, and bottom contact layers, respectively. The top-contact layer is etched down leaving a 0.1 μm thick region inside the ring contact. The UV active layer thickness was increased to 1.2 μm from 0.6 μm used in the previous detectors in order to block more of the UV radiation. The fraction of UV radiation transmitted through the top-contact layer and the electrical field distribution across the AlGaN barrier is considered to determine the required top-contact thickness. Hence, a zero or extremely low UV response from the IR active region was expected as almost all the UV radiation should be absorbed in the 1.2 μm AlGaN region. However, as can be seen from Fig. 2.7, if a broad light spot is incident on to the entire detector structure, there can be some UV light penetrating into the IR-active region. This is due to the small opening between the middle metal contact and the side wall of the top layers as shown in Figs. 2.7(b) and (c).

In fact, new masks have been applied to block the leakage of UV radiation into the IR-active region. This will eliminate the need for an external aperture. In order to block the leakage, the metal coverage of the MC was extended in order to cover the edges of the mesas from the top to middle and middle to bottom contacts. To achieve this without making unwanted contact to the mesa sides, an insulating layer was first laid down reaching from the MC layer up to the metal on the TC layer and from the MC layer down to the metal on the BC layer as shown in Fig. 2.8. The metal for the MC was then deposited on these insulating layers extending from over the TC to over the BC (see Fig. 2.8). Any incident UV radiation would then be blocked by the metal of the MC except for the window opening through the top contact metal for the measurements.

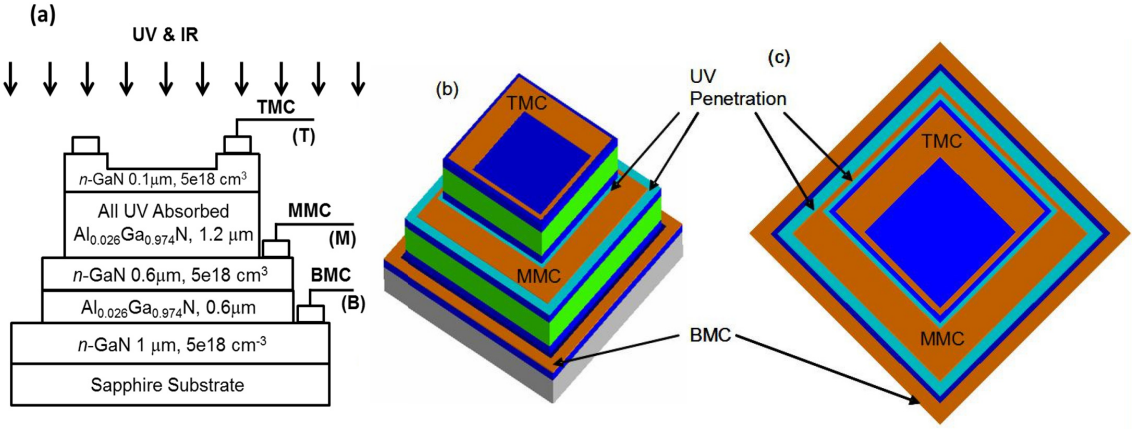

Figure 2.7 (a) The thickness of the AlGaN layer in the UV active region is set to 1.2 μm in order to block any UV radiation transmitting into the IR active region from the top. (b) A 3D view showing the top, middle, and bottom contacts with the metalization. (c) The top view showing the open area that light can pass through for the top contact layer (dark shading) and the middle contact layer (light shading).

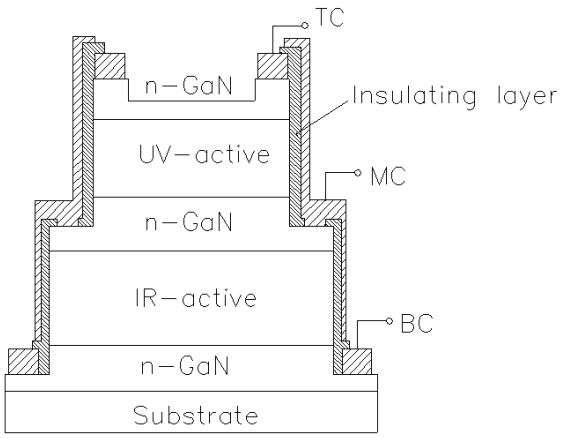

Figure 2.8 The new processing to block the UV radiation leakage into the IR-active region. The labels TC, MC, and BC indicate the top-, middle-, and bottom-contacts, respectively

2.6 Further Improvements to UV and IR Performance

As can be seen in Fig. 2.6 the UV-active region has low dark current especially under negative bias. This dark current is mainly determined by thermionic emission over the work function at the top emitter/barrier interfacial work function. This dark current can be further reduced (even at high operating temperatures) by increasing this interfacial work function by increasing the Al composition in the barrier, hence leading to higher D*. However, this will shift the UV threshold into deep UV region. In addition, the UV response can be further increased by increasing the thickness of the AlGaN layer in order to absorb almost all of the UV passing through the top AlGaN layer. Furthermore, the thickness of the top contact layer can be reduced to decrease the unwanted absorption in the top contact layer. This will allow more light passing into the AlGaN layer. However, this can introduce a non-uniform electric field. Directly depositing interdigitated contacts on top surface of the detector can improve the electric field uniformity.[39, 40] Interdigitated contacts can be directly deposited on the AlGaN layer in the UV-active region without using an n^+-GaN top contact layer.[41] This will allow the generation of a lateral applied electric field. Having a lateral contact geometry[39] will avoid the need for carriers to pass through the GaN/AlGaN interface, hence reducing the hole trapping. In addition, a *p-i-n* structure[42] for UV-active region can be considered as another possibility. In the *p-i-n* structure, the dark current is expected to be low,[42] since the excited free holes in the top-contact cannot travel toward the middle-contact due to high potential barrier.

In order to improve the IR performance of the detector, additional periods of n^+-GaN/AlGaN might be added in the IR-active region. Moreover the IR threshold can be shifted to shorter wavelength. This will reduce the dark current and increase the operating temperature of the detector. In addition, graded barriers in the HEIWIP structure can be used to have photovoltaic operation,[43] requiring low power and having reduced low frequency noise. As reported for similar GaAs/AlGaAs HEIWIP IR detectors,[43] these detectors have high D^*. They exhibit no thermally assisted tunneling currents, and hence

higher operating temperatures. Furthermore, intervalence band absorption (IVB) of p-GaN can be useful to extend the IR threshold to far-IR region ($\lambda > 60\mu m$) with better performance. However, due to the low work function for HEIWIP structures in the far-IR region, the detector performance can be affected by the high dark current at higher temperatures. This concept of having additional response due to IVB absorption on top of free carrier absorption is demonstrated using p-GaAs based HEIWIP detectors,[44] which operates at or around room temperature with high D^*. Another possibility is to implement GaN/AlGaN Quantum Well Infrared Photodetectors (QWIPs). It has been shown[45] that GaN/AlGaN QWIPs having threshold wavelengths up to 6 μm (with broad spectral peaks) which can be operated at room temperature. The threshold wavelength can be extended to longer wavelength with further modifications to the QWIP structure.

2.7 Conclusion

Results were presented for a GaN/AlGaN single element detector capable of simultaneously and separately identifying both the UV (250 - 360 nm) and IR (5 - 14 μm) responses with near zero spectral cross talk. The detector consists of separate UV- and IR-active regions with separate electrical contacts. The UV response is based on interband transitions in the undoped barrier layer, while the IR response is due to intraband transitions (free carrier absorption) in the emitter followed by photoemission across emitter/barrier interface. The thresholds of the UV and IR responses can be tailored by adjusting the Al fraction. Interestingly, shorter UV thresholds (deep UV detection) will give lower dark currents due to the higher band offset between the top contact and AlGaN layer. In addition, interdigitated contacts can be directly applied on the AlGaN layer[41] to get rid of the unwanted abosorption in the top n-GaN layer. The IR response can be further improved by the addition of more periods of GaN/AlGaN in the IR-active region. The operating temperature of the IR-active region can be increased by shifting the IR threshold to shorter wavelength. In addition, GaN/AlGaN QWIPs can also be implemented to achieve higher operating temperatures. Furthermore, IVB absorption in p-GaN could be used to improve far-IR response.

CHAPTER 3

SEMICONDUCTOR MATERIAL CHARACTERIZATION BY INFRARED REFLECTANCE, TRANSMISSION, AND ABSORPTION SPECTROSCOPY

3.1 Introduction

Optical characterization techniques are useful and widespread tools for semiconductor material characterization, as they are non-destructive. Commonly used optical characterization methods include reflectance, transmission, and absorption spectroscopies in UV-VIS-IR, Raman spectroscopy, and Photoluminescence (PL) spectroscopy. These techniques are used to investigate important electrical and optical properties of semiconductor materials without damaging the materials. IR reflectance and transmission spectroscopy is mainly used to investigate the bandgap, Dielectric function, phonon and plasmon properties, carrier concentrations, carrier mobility, layer thicknesses, and interface behavior.

3.2 Modeling reflection, transmission, and absorption in multilayer semiconductor structures

The well-known transfer-matrix method[46, 47] can be used to model light propagation in a multilayer thin film structure. Figure 3.1 (b) shows the normal incident light propagation through an isotropic and homogeneous multilayer structure. In a given layer, light propagates in both $+z$ and $-z$ directions due to the multiple reflections, and E^+ and E^- indicate the electric fields of light in the $+z$ and $-z$ directions. At the interface between i^{th} and $(i+1)^{th}$ layers [see Fig. 3.1 (a)], the electric fields satisfy the following conditions

$$E_i^+ + E_i^- = E_{i+1}^+ + E_{i+1}^- \tag{3.1}$$

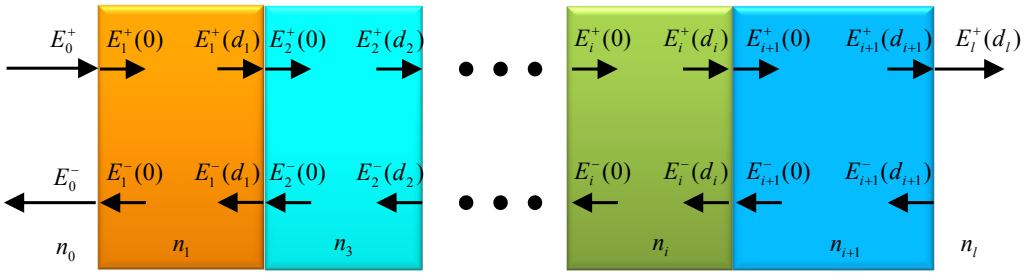

Figure 3.1 Normal incident light propagation in a multilayer stack with l number of layers are shown. The medium for each layer is considered as isotropic. The directions of the electric fields (E)are shown with arrows. The forward and backward traveling light components exist due to the multi-reflections at each interface. Here, n_i and d_i are the complex refractive index and the thicknesses of the i^{th} layer. The electric field of incident light and reflected light are E_0^+ and E_0^-, respectively. The electric field transmitted by the multilayer stack is $E_l^+(t_l)$.

Using Eq. 3.1 the electric fields of propagating light inside the $(i+1)^{th}$ layer can be expressed in terms of the electric fields in the i^{th} layer. The $+z$ direction electric field in $(i+1)^{th}$ layer is

$$E^{+}_{i+1}(0) = \frac{1}{2}[(1+\frac{n_i}{n_{i+1}})E^{+}_{i}(d_i) + (1-\frac{n_i}{n_{i+1}})E^{-}_{i}(d_i)], \tag{3.2}$$

The $-z$ direction electric field in $(i+1)^{th}$ layer is

$$E^{-}_{i+1}(0) = \frac{1}{2}[(1-\frac{n_i}{n_{i-1}})E^{+}_{i}(d_i) + (1+\frac{n_i}{n_{i+1}})E^{-}_{i}(d_i)], \tag{3.3}$$

where n_i and d_i are the complex refractive index and the thickness of the i^{th} layer, respectively. Now, Eq. 3.2 and Eq. 3.3 can be expressed in a matrix format as shown in Eq. 3.4.

$$\begin{pmatrix} E^{+}_{i+1}(0) \\ E^{-}_{i+1}(0) \end{pmatrix} = T_{i,i+1} \begin{pmatrix} E^{+}_{i}(d_i) \\ E^{-}_{i}(d_i) \end{pmatrix}, \tag{3.4}$$

where T is the transfer-matrix for light propagation from the i^{th} layer into the $(i+1)^{th}$ layer,

$$T_{i,i+1} = \begin{pmatrix} 1+\frac{n_i}{n_{i+1}} & 1-\frac{n_i}{n_{i+1}} \\ 1-\frac{n_i}{n_{i+1}} & 1+\frac{n_i}{n_{i+1}} \end{pmatrix}.$$

The electric fields propagating inside the i^{th} layer are given by Eq. 3.5

$$\begin{pmatrix} E^{+}_{i}(x_i) \\ E^{-}_{i}(x_i) \end{pmatrix} = P_i \begin{pmatrix} E^{+}_{i}(0) \\ E^{-}_{i}(0) \end{pmatrix}, \tag{3.5}$$

where, $P_i = \begin{pmatrix} e^{ikn_ix_i} & 0 \\ 0 & e^{-ikn_ix_i} \end{pmatrix}$ and is called the propagation-matrix. Light transmission from one layer to another layer and light propagation inside each layer can be expressed by separate transfer-matrices and separate propagation-matrices defined for each layer. Therefore, the electric fields in the j^{th} layer can be written in terms of the initial electric fields E^{+}_{0}

and E_0^- as

$$\begin{pmatrix} E_j^+(0) \\ E_j^-(0) \end{pmatrix} = \begin{pmatrix} a & b \\ c & d \end{pmatrix} \begin{pmatrix} E_0^+ \\ E_0^- \end{pmatrix}, \tag{3.6}$$

where $\begin{pmatrix} a & b \\ c & d \end{pmatrix} = \begin{pmatrix} 1+\frac{n_{j-1}}{n_j} & 1-\frac{n_{j-1}}{n_j} \\ 1-\frac{n_{j-1}}{n_j} & 1+\frac{n_{j-1}}{n_j} \end{pmatrix} \begin{pmatrix} e^{\phi_{j-1}} & 0 \\ 0 & e^{-\phi_{j-1}} \end{pmatrix} ...$

$$... \begin{pmatrix} e^{\phi_1} & 0 \\ 0 & e^{-\phi_1} \end{pmatrix} \begin{pmatrix} 1+\frac{n_0}{n_1} & 1-\frac{n_0}{n_1} \\ 1-\frac{n_0}{n_1} & 1+\frac{n_0}{n_1} \end{pmatrix}$$

and $\phi_i = ikn_it_i$ is the phase angle.

Finally, the incident ($E_i = E_0^+$), reflected ($E_r = E_0^-$), and transmitted (E_t) electric field components for the whole multilayer structure can be formulated as given in Eq.3.7.

$$\begin{pmatrix} E_t \\ 0 \end{pmatrix} = M \begin{pmatrix} E_i \\ E_r \end{pmatrix}, \tag{3.7}$$

where M is the product of all transfer- and propagation-matrix multiplication from the 1^{st} layer through the last layer l^{th} and is given by $M = \begin{pmatrix} A & B \\ C & D \end{pmatrix} = T_l \cdot P_{l-1} ... P_i \cdot T_i ... P_1 \cdot T_1$

Now, reflectance (r) and transmittance (t) can be written as in Eq. 3.8 and Eq. 3.9,

$$r = \frac{E_r}{E_i} = \frac{-C}{D} \tag{3.8}$$

$$t = \frac{E_t}{E_i} = A + \frac{BC}{D} \tag{3.9}$$

Therefore, reflection (R) and transmission (T) can be calculated as follows,

$$R = r^* r, \tag{3.10}$$

$$T = t^* t \frac{n_l \mu_0}{n_0 \mu_l}, \tag{3.11}$$

where n_0, n_l, μ_0, and μ_l are the complex refractive indices and the permeabilities of the media that incident light starts in and the transmitted light exits into. If the starting and the final media are the same, then $T = t^* t$. Finally, the total light absorption (A) inside the whole multilayer stack can be obtained as

$$A = 1 - (R + T). \tag{3.12}$$

3.3 IR dielectric function of *p*-InP

Indium Phosphide is a basic semiconductor material for infrared (IR) optoelectronic and photonic device fabrication developed for future optical communication systems. The development of group-III Phosphide based optoelectronic devices[48] depends on understanding the optical properties of Phosphide materials and their alloys with doping and temperature. In a p-type InP semiconductor where free holes are present, inter-valence band (IVB) transitions can occur among the split-off (so), light-hole (lh) and heavy-hole (hh) bands each with two-fold spin degeneracy. Recent studies on p-type semiconductors have attracted attention for optical studies on the absorption properties using infrared dielectric function (DF)[10] as well as applications to heterojunction internal photoemission detectors.[44] Recently reported, GaAs based internal photoemission type detectors[44, 49] have shown high operating temperature (up to 330 K) capability in 1 - 3 μm and 8 - 14 μm IR wavelength ranges. Since IVB and free carrier (FC) absorption depends on the concentration of free holes and the spin-orbit splitting energy of p-InP[50] is 108 meV, the total absorption coefficient of heavily doped InP can be higher than that of other materials such as p-GaAs. Therefore, a model dealing with the IVB transitions will be of interest for practical applications as well as for fundamental research. Furthermore, accurate simulation and design of device structures need proper handling of doping effects including the IVB transitions for calculating optical constants. In this work, a DF model that takes into account IVB transitions

was deduced with analytical expressions under the parabolic-band approximation.[51] Recent implementation of p-InP waveguides which provide better current blocking in Quantum Cascade Lasers (QCLs)[52] attracted attention for optical studies on the absorption and refractive index properties. Infrared absorption in GaP[53] and InP[54] bulk crystals has been reported previously using two-phonon absorption spectroscopy, and these papers also discuss the effect of higher order terms of the primary phonons of those materials. A few studies have been reported based on density matrix theory[55] in the near-IR (1 - 3 μm) region for InP epitaxial films. However, detailed mid (3 - 14 μm) and far (14 μm and beyond) IR absorption (experimental or theoretical) studies for p InP epitaxial films have not been reported, and also have not been modeled using the DF. Determination of crystalline quality and the FC concentration can be characterized from plasma frequency[56] and phonon mode dependency on polarized light[57] incident at oblique angles.

3.4 Experiment

The p-type InP epitaxial films were grown on semi-insulating, InP substrates by gas source molecular beam epitaxy (GSMBE), for high (2.4×10^{19} cm^{-3}) doping and metal organic vapor phase epitaxy (MOVPE) for low (1 and 3×10^{18} cm^{-3}) doping. The thickness of the substrate is 350 μm for GSMBE and 440 μm for MOVPE grown samples. The samples were back side polished in order to reduce the reflection losses and scattering from the surface. All measurements were performed with a Perkin-Elmer system 2000 Fourier transform infrared spectrometer (FTIR) along with a globar source, a HgCdTe detector with a KBr beamsplitter (for mid-IR), and a Triglycine Sulphate (TGS) detector with a 6 micron mylar beamsplitter (for far-IR). The spectral resolution was 4 cm^{-1}. For both the substrate sample and the film/substrate samples, transmittance was measured under normal incidence, while the reflectance was measured at near normal incidence with a gold mirror as a reference using the specular reflection accessory at room temperature. A helium closed cycle refrigerator system was used for the measurements from 25 to 275 K at 25 K intervals.

3.5 Theoretical Models

The DF in the IR region is primarily determined by phonon and FC contributions.[58] The phonon contribution arises from collective lattice vibrational modes under the propagating electric field of the incident light. These phonon contributions are modeled using Lorentz oscillators. The FC plasma contribution, which is due to the interaction of FC with the electric field of the incident light, can be modeled using the classical Drude model[59] approximation. It has been successfully applied to p-GaAs[60] and n-GaN[61] using a single plasma frequency and damping constant along with a Lorentzian oscillator model. Hence, the DF can be presented in Eq. 3.13 for the IR region,

$$\epsilon(\omega) = \epsilon_\infty \left(1 - \frac{\omega_p^2}{\omega_p^2 + i\omega\gamma}\right) + \sum_j \frac{S_j \omega_{f,j}^2}{\omega_{f,j}^2 - \omega^2 + i\omega\Gamma_j} \tag{3.13}$$

where ω, ω_p, γ and ϵ_∞ are the frequency of the incident light, the FC plasma frequency, the FC plasma damping factor, and the high frequency dielectric constant, respectively. Also, $\omega_{f,j}$, S_j and Γ_j are the frequency of the jth Lorentzian oscillator (which represents the corresponding phonon frequency), oscillator strength, and oscillator broadening. Here, S_j and ϵ_∞ are unitless and other terms have the unit of cm^{-1}.

The intensity-transfer-matrix method[62] was used to calculate the IR reflectance and transmittance spectra from the three phase vacuum/film/substrate multilayer structure. The interface matrix ($\mathrm{Q}_{j\text{-}1,\,j}$) which represents the interaction of light between the *(j - 1)*th and jth layers is given by

$$Q_{j-1,j} = \frac{1}{2\sqrt{\epsilon_{j+1}}} \begin{bmatrix} \sqrt{\epsilon_j} + \sqrt{\epsilon_{j-1}} & \sqrt{\epsilon_j} - \sqrt{\epsilon_{j-1}} \\ \sqrt{\epsilon_j} - \sqrt{\epsilon_{j-1}} & \sqrt{\epsilon_j} + \sqrt{\epsilon_{j-1}} \end{bmatrix} \tag{3.14}$$

and the propagation matrix (P_j) for the light propagation in the jth layer with thickness d is described by

$$P_j = \begin{bmatrix} \exp(i2\pi\sqrt{\epsilon_j}d/\lambda) & 0 \\ 0 & \exp(-i2\pi\sqrt{\epsilon_j}d/\lambda) \end{bmatrix} \tag{3.15}$$

The electric and magnetic fields in each layer can be obtained by repeating Eq. 3.14 and 3.15. The total transfer matrix, M is the multiplication of the matrix in layer 0 through layer N ($j = 0$ representing the light incoming media), i.e., $M = \prod_{j-1}^{N} P_j Q_{j-1,j}$. The reflectance ($R$) and transmittance ($T$) are expressed by

$$R = \left| \frac{M_{21}}{M_{11}} \right|^2$$

and

$$T = \frac{Re(\sqrt{\epsilon_N})}{Re(\sqrt{\epsilon_0})} \left| \frac{\det(M)}{M_{11}} \right|^2 \tag{3.16}$$

The multiple reflected beams from the substrate surfaces are added incoherently to neglect the phase information as described in Ref. [63]. Hence, the Eq. 3.16 is modified accordingly.

The reflection and transmission spectra for the doped samples are shown in Fig. 3.2. The absorption spectra for all the samples are shown in Fig. 3.3. The transmission in 30 - 35 μm range is near zero; hence not shown in the figure. There is a step around 20 μm as can be seen in reflection, transmission and absorption spectra (see Figs. 3.2 and 3.3) which is similar to that for GaAs[64] and due to multi-phonon absorption. This feature is a consequence of the substrate's transparency below 20 μm that allows a contribution to the observed reflectivity from light returning from the substrate's back surface which is in agreement with the theoretical model (especially for highly doped samples). However, the mismatch between calculated and experimental data around this feature will not affect the other results. The small difference is due to the Lorentzian shape of the oscillators. Due to phonon absorption and the Reststrahlen effect (imaginary part of the dielectric function becomes larger), transmission decreases above 20 μm.

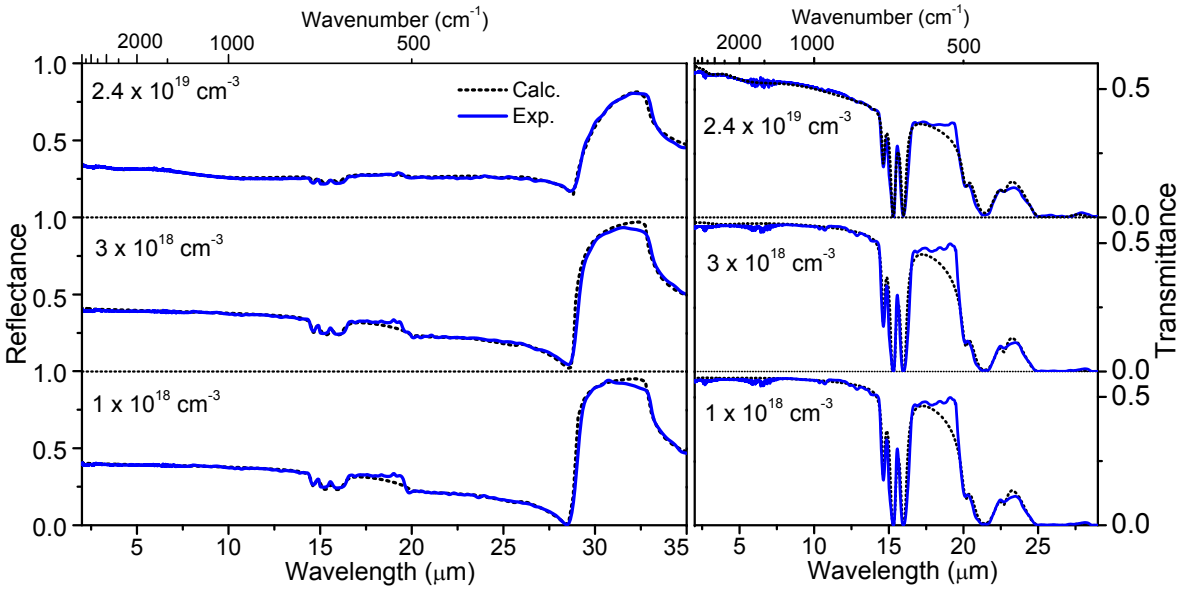

Figure 3.2 Experimental reflectance and transmittance spectra (dotted lines) of the sample having p-InP epilayers on InP substrate along with the best fit results (solid lines) at 300 K. The transmission drastically reduces beyond 20 μm and is almost zero in 30 - 35 μm range. Therefore this region for transmission is not shown. The top axis represents wavenumber (cm^{-1}) scale which is equal to $10{,}000/\lambda(\mu\mathrm{m})$. Doping densities are also shown for each sample.

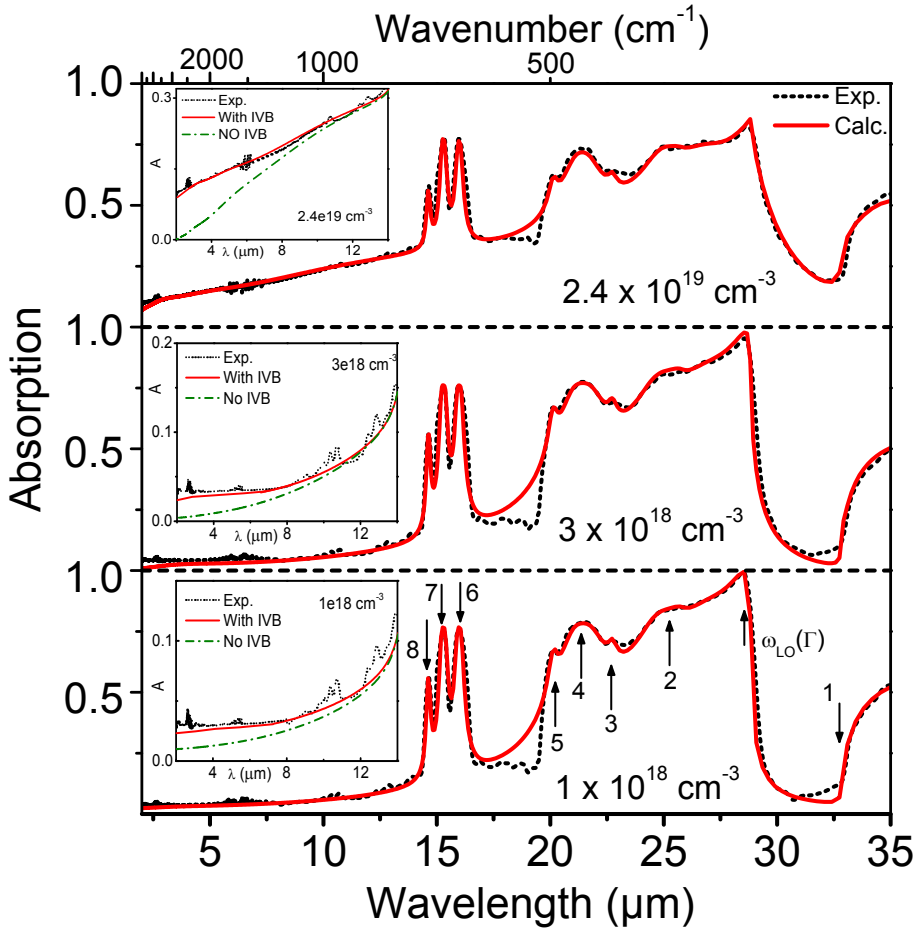

Figure 3.3 Experimental absorption spectra (dotted lines) of the p-InP films on InP substrate along with their best fit results (solid lines) at 300 K. The arrows indicate the location of each Lorentzian oscillator. The insets show the enlarged region (2 - 14 μm) where IVB absorption is expected, which show the absorption with and without IVB transitions. The IVB absorption increases with doping and over-shadows the weaker higher order phonon peaks in 10 - 13 μm range.

Even though there are many higher order phonon frequencies[53] associated with InP material, only eight Lorentz oscillators (as shown by arrows in Fig. 3.3) were implemented to study the phonon absorption depending on their strength in absorption. The oscillator parameters for the substrate are given in Table 3.1. The first oscillator is the primary transverse optical (TO) phonon in InP and other oscillators are assigned to different combinations of TO and longitudinal optical (LO) phonons at different critical points in the Brillouin zone as given in Ref. [54]. The best-fit parameter values in Eq. 3.13 are found using a Levenberg-Marquardt algorithm.[65] The reflectance and transmittance spectra were used to derive $\epsilon(\omega)$ using the fitting procedure. The value of $\epsilon_\infty(9.6)$ was taken as a fixed parameter.[55] The ω_p for FC with effective mass (m^*) and carrier concentration (np) can be found by

$$\omega_p = \sqrt{\frac{pe^2}{\varepsilon_0 \varepsilon_\infty m^*}} \Big/ 2\pi c \tag{3.17}$$

. SI units should be used with this equation. Here, e is the electron charge and c is the speed of light. The value of m^* is taken as an average of hh and lh masses,[66] $(m_{lh}^{3/2}+m_{hh}^{3/2})/(m_{lh}^{1/2}+m_{hh}^{1/2})$, where ($m_{hh}^*$=0.58 and m_{lh}^*=0.12).[67] n_p was obtained from Hall measurements and is used as the initial value in the fitting program and the final ω_p values extracted from the fittings are listed in Table 3.2. The oscillator/phonon frequencies of the semi-insulating InP substrate were initially determined by cross-referencing the values reported[54] for bulk InP. Once those frequencies were fixed, the oscillator strength and broadening parameters were optimized for the first oscillator, since it is the strongest.[54] These parameters determine the shape of the reflectance spectra mainly in the far-IR region (26 - 35 μm) and increase with doping (as listed in Table 3.2). The parameters for the other oscillators were optimized using both reflectance (R) and transmittance (T) spectra. The spectra are shown in Fig. 3.2. The IR absorption was calculated from $A = 1 - T - R$ and is shown in Fig. 3.3 for different doping levels. The variation of strength and broadening values for other oscillators due to doping is within the tolerance of the fitting parameters.

Table 3.1 Fitting parameters for each Lorentz oscillator of semi-insulating InP substrate at 300 K. Here ω_p, S, and Γ are phonon frequency, oscillator strength, and broadening constant, respectively, as given in Equation 3.13. Best-fit 90% confidence limits are given in parentheses.

	Oscillator number							
	1	2	3	4	5	6	7	8
ω_f (cm^{-1})	305.5 (0.5)	386.0 (0.5)	440.0 (0.5)	467.1 (0.5)	496.5 (0.5)	625.5 (0.5)	654.0 (0.5)	683.3 (0.5)
S_f	2.78 (1e-2)	0.022 (1e-3)	0.0002 (1e-4)	0.004 (1e-3)	0.0003 (1e-4)	0.001 (1e-3)	0.001 (1e-3)	0.0002 (1e-4)
Γ_f (cm^{-1})	1.1 (0.5)	12 (1)	8 (1)	25 (2)	10 (1)	6.5 (1)	6 (1)	8 (1)
Ref.	$TO(\Gamma)$	$TO(X)$+ $TA(X)$	W_3 + W_4	W_1 + W_4	$LO(L)$+ $LA(L)$	$2TO(L)$	$LO(\Gamma)$+ $TO(\Gamma)$	$2LO(L)$

Table 3.2 Fitting parameters for computing the contributions of FC, phonon absorption, and IVB transitions to the DF (at 300 K). Here, d, ω_p, and γ are thickness of the epi-layer, FC plasma frequency, and FC plasma damping, respectively. S_1 and Γ_1 are strength and broadening of the first oscillator. A and Γ are the strength and broadening for each IVB transition. The first column shows the nominal doping values from Hall measurements. Best-fit 90% confidence limits are given in parentheses.

Sample (cm^{-3})	d (nm)	ω_p (cm^{-1})	γ (cm^{-1})	S_1	Γ_1 (cm^{-1})	A_{lh-hh} (meV^2cm^3)	A_{so-hh} (meV^2cm^3)	Γ_{ll-hh} (meV)	Γ_{so-hh} (meV)
2.4×10^{19}	1190	649	1318	3.10	1.7	2.1	1.2	102	110
	(2)	(3)	(9)	(0.01)	(0.5)	(0.2)	(0.1)	(5)	(2)
3×10^{18}	675	252	512	2.82	1.2	1.9	1.1	43	72
	(2)	(3)	(8)	(0.01)	(0.5)	(0.2)	(0.1)	(5)	(2)
1×10^{18}	675	144	304	2.80	1.1	1.9	1.1	22	13
	(2)	(3)	(8)	(0.01)	(0.5)	(0.2)	(0.1)	(5)	(2)

3.5.1 Intervalence band transitions

The intervalence band (IVB) transitions yield an additive contribution to the dielectric function. For p-type semiconductors, three IVB transitions can occur among the valence bands (split-off (so), light-hole (lh), and heavy-hole (hh) bands). I adopt an approximation of using parabolic-band structures, which is valid for most of the doping concentrations since the transitions primarily occur around the Γ point. The modeling details have been described in Ref. [10]. The following analytic expressions are given only for the imaginary component, and the real component is obtained from the Kramers-Kronig transformations. The IVB contribution to the dielectric function can be expressed by,[10]

$$\epsilon_2(E) = \epsilon_2^{12}(E) + \epsilon_2^{13}(E) + \epsilon_2^{23}(E) \tag{3.18}$$

.

Here, superscripts denote the three different bands and subscript denotes the imaginary part of the dielectric function. For a transition taking place between bands a and b (a, b = so, lh, hh, the DF is given by

$$\epsilon_2^{ab}(E) = \frac{A_{ab} p \left|E - (E_{b0} - E_{b0})\right|^{3/2}}{E^2 (k_B T)^{3/2}} \left(\exp \frac{E_a}{k_B T} - \exp \frac{E_b}{k_B T}\right) C_{FD}^{ab} \tag{3.19}$$

where p is the hole concentration, k_B is the Boltzmann constant, T is the temperature, and $E_{a(b)}$ is given by the parabolic band form, $E_{a(b)} = -E_{a(b)0} - \hbar k^2 / 2m^*_{a(b)}$ with $E_{a(b)}$ and m^* being the band-edge energy and being the effective mass for band *a(b)*. In Eq. 3.19, E_a and E_b are determined by $E_a - E_b = E$, and A_{ab} accounts for the transition strength and other effects such as the non-parabolicity of energy bands of the Γ point. The model fits[10] to the p-GaAs data show that A_{ab} is constant except at the higher doping range above 10^{19} cm^{-3} as a result of the band non-parabolicity. Here, A_{ab} is expressed as

$$A_{ab} = \frac{16 C_0 B_{ab}}{\hbar (m_a^{*3/2} + m_b^{*3/2})} \left(\frac{\pi m_a^* m_b^*}{m_a^* - m_b^*}\right)^{5/2} \tag{3.20}$$

C_{FD}^{ab} is a constant related to the Fermi level,

$$C_{FD}^{ab} = \frac{\exp\left\{-\left[E_f + k_B T)\ln\frac{P}{N_v}\right]/k_B T)\right\}}{\{1+\exp\left[(E_a - E_f)/k_B T)\right]\}\{1+\exp\left[(E_b - E_f)/k_B T)\right]\}} \tag{3.21}$$

where E_f is the energy of the hole quasi-Fermi level and N_v is the sum of *hh* and *lh* effective density of states. For low doping concentrations, E_f lies above the VB top, yielding $C_{FD}^{ab} \approx 1$. The non-parabolicity in the actual VBs of the Γ point causes m^* and A_{ab} to vary. At wave vectors where hole transitions will see the parallel bands, A_{ab} can be significantly increased.

3.6 Results and Discussion

To obtain the IVB DF, parameters representing the strength (A_{ab}) and line-shape broadening (Γ_{ab}) of transitions were determined by fitting experimental data with the model output. Compared to p-GaAs,[10] the case of p-InP is complicated by the small spin-orbit splitting ($\Delta_{so} = 108$ meV). Therefore, *so-hh* and *lh-hh* absorption regions are merged, unlike the case for *p*-GaAs. Because of this small *so* value, much of the absorption due to direct IVB transitions occurs in a region of the IR where lattice absorption and FC absorption are strong. Based on the DF model in Ref. [10], a fit to the absorption spectra is shown in Fig. 3.3. The fitting parameters are given in Table 3.2. The insets in Fig. 3.3 show the absorption with and without IVB transitions in the 2 - 14 μm region. This shows that the differences are due to the IVB transitions. It can also be seen that IVB absorption increases with doping. The small absorption peaks visible (10 - 13 μm range) are due to higher order phonon frequencies[53] and are prominent in low doping samples. In view of these results, the *so-hh* and *lh-hh* transitions have a larger broadening constant for higher doping levels. This is reasonable since the energy of transitions occurring around the Fermi surface shifts toward higher values. The result is a large quantity of holes being populated into the higher energy states. The *so-lh* transition is relatively weak due to the low occupation of the holes in the *lh* band.[10] The strength of the IVB transitions is controlled by the concentration of the free holes and is in competition with intra-band FC absorption. The total absorption

coefficient extracted from the DF is plotted in Fig. 3.4 with comparisons to the experimental[1] data for a doping density of 1 $\times 10^{18}$ cm^{-3}. The reason for higher values in absorption coefficient in the MIR region is that the substrate is more optically thick compared to the doped thin film layer.

The temperature dependence of ω_p, γ, and the phonon frequencies has been studied from 25 to 300 K as shown in Fig. 3.5. The empirical formula deduced is

$$\omega_p = \omega_0 + a_1 \exp(-1000/Tb_1) \tag{3.22}$$

where $a_1 = 107$,

$$b_1 = 1.75 + 0.008(n_p/10^{18}), \tag{3.23}$$

and

$$\omega_0 = 20.8 + 137.2(n_p/10^{18}). \tag{3.24}$$

Here, n_p, ω_p, and T are in cm^{-3}, cm^{-1}, and Kelvin, respectively. According to this equation the plasma frequency decreases exponentially with decreasing temperature. The parameters are given in terms of hole concentration (n_p) at 300 K. Free carrier intra-band (same energy band) absorption is an indirect process and is mediated by phonons [68] which supply the additional momentum required for the overall energy and momentum conservation and are responsible for the temperature dependence of optical features. Also, ω_p depends on hole density and hole effective mass. Since the damping and plasma frequency are interconnected, the fitting parameters for damping are given in terms of the fitting parameters of plasma frequency. Therefore, an empirical formula deduced for plasma damping is

$$\gamma = \gamma_0 + a_2 \exp(-1000/Tb_2) \tag{3.25}$$

where

$$a_2 = 1.72a_1 + 5.26(n_p/10^{18}), \tag{3.26}$$

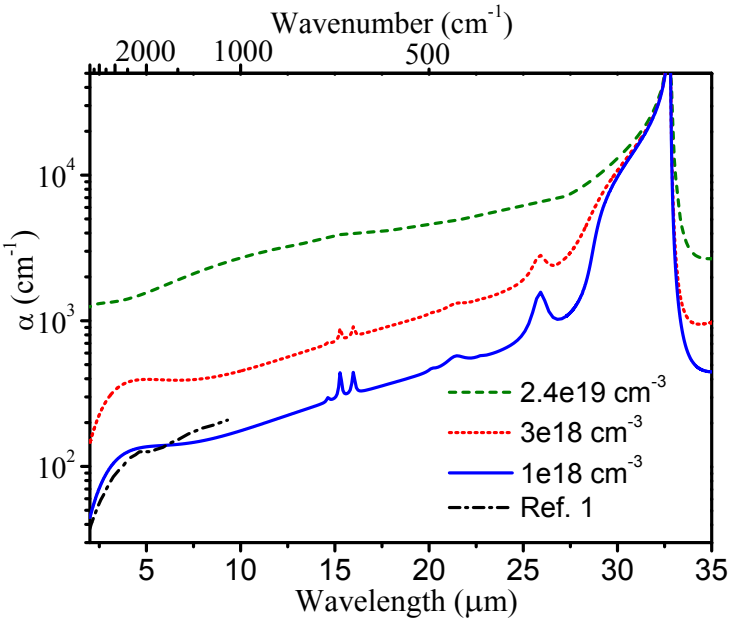

Figure 3.4 Calculated absorption coefficient at 300 K. The strong absorption peak around 32.7 μm (306 cm^{-1}) is due to Reststrahlen absorption of the lattice structure. The weak peaks are due to the difference in phonon absorption between the doped layer and the substrate. The theoretical values are compared with the data taken from Ref. [1] for a doping density of 1×10^{18} cm^{-3}.

$$b_2 = 4.76 + 1.15b_1, \tag{3.27}$$

and

$$\gamma_0 = 11.49 + 2.28\omega_0. \tag{3.28}$$

This indicates that at low temperature, the mobility of free carriers increases. The saturation level at low temperatures is given by ω_0 and γ_0. In addition, the phonon frequencies blue shift with decreasing temperature (ω_f = 633 - 0.02T). Even though Raman measurements [69] of the temperature dependence of phonons indicate that this dependence is not linear for oscillator #1, the linear approximation for phonon frequency shift is good enough to describe the results in mid-infrared region for oscillators #6, #7, and #8. The temperature dependence of these phonons is shown in the inset of (b). The low temperature measurements were not carried out in the far infrared region ($\lambda > 22$ μm) where oscillator #1 is located.

The effective mass of holes is an important parameter that affects the mobility, electrical resistivity, and free-carrier optical response of a semiconductor. Most commonly, their effective mass is simply designated by their values at their respective band edges. However, for high carrier concentrations or under cryogenic temperatures, the effective masses can vary significantly from their band-edge values. These variations are due to the characteristics of the semiconductor band structure, such as nonparabolicity and the splitting of the bands at valence band edges. Although there have been a few theoretical attempts to understand the temperature dependence of the effective mass,[70] experimental studies for cryogenic temperatures are not yet reported for p-InP. The calculated density of states and hole effective mass reported in Ref. [70] shows a 50 % increase from room temperature to 80 K for a doping density of 1×10^{18} cm^{-3}. Due to the large density of states, heavy holes play a dominant role in optical transitions. The valence bands in III-V compounds are warped from spherical symmetry, and it has been shown that, depending on the method of measurement, heavy-hole mass values ranging from $0.3m_0$ to $0.8m_0$ are obtained from theoretical studies for InP.[71] A good review of theoretical and experimental evaluations of the InP hole ef-

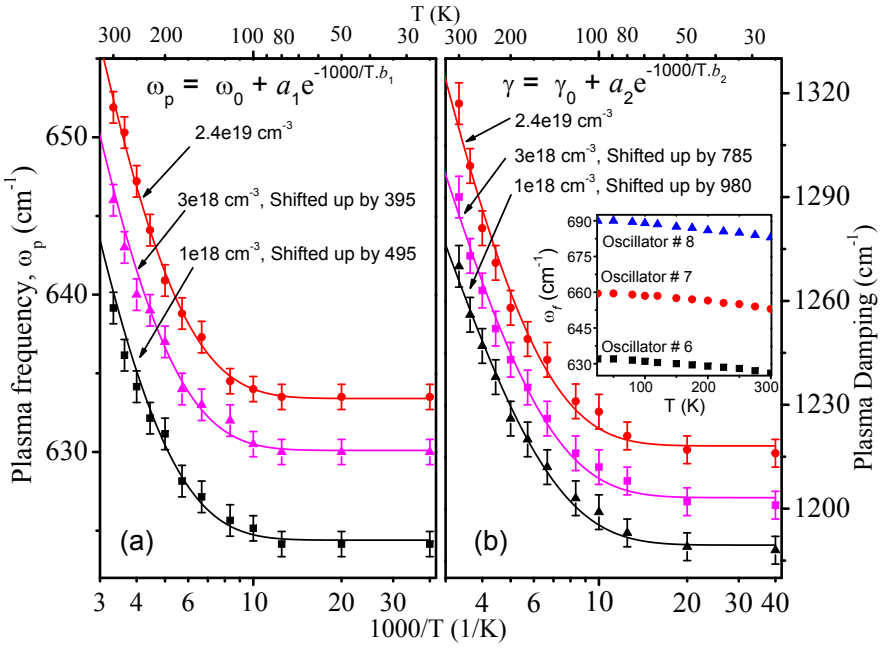

Figure 3.5 The temperature dependence of (a) plasma frequency ω_p and (b) plasma damping factor γ is shown. Solid lines are the best fits to the experimental data. Data for two of the lowest doped samples are shifted up for comparison. The parameters used in empirical formulas (shown in the figures) depend on the 300 K carrier concentration. ω_0 and γ_0 indicate the saturation level at low temperatures. The inset in (b) shows the variation of phonon frequency with temperature.

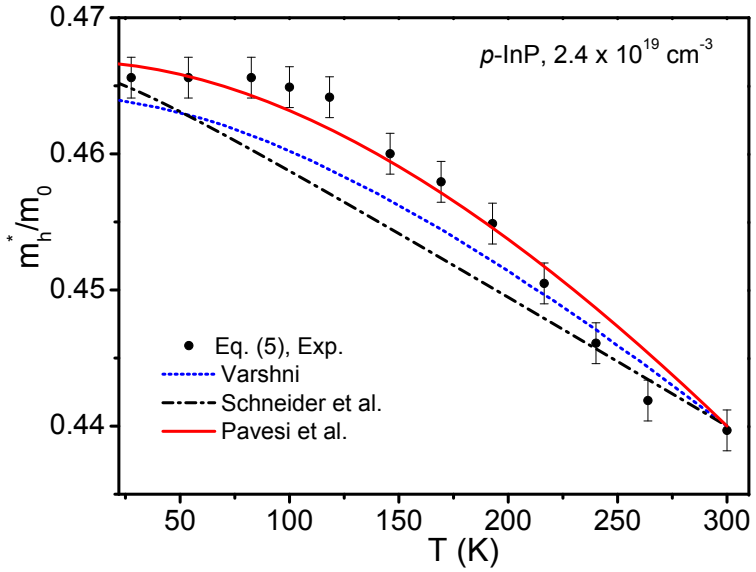

Figure 3.6 The hole effective mass (m_h^*) extracted from plasma frequency (ω_p) using Eq. 3.17 is plotted for different temperatures for the highest doped sample (2.4×10^{19}) is shown by dots with error bars. The calculated values for m_h^* using Eq. 3.29 are also shown for different bandgap variation cases: Schneider et al.[2], Varshni[3], and Pavesi et al.[4].

fective mass at room temperature is given in Ref. [71]. In our work, the plasma frequency variation at different frequencies has been used to extract the effective mass dependency with temperature, assuming that plasma frequency change is mainly due to a change in the effective mass. This is shown in Fig. 3.6 for the highest doped sample (dots). The effective mass increases by 5 % as the temperature is lowered from 300 to 100 K. The effective mass stays constant for temperatures below 100 K. Since there are no experimental data reported at low temperature to the best of our knowledge, I compare our results with two theoretical methods as described below.

The hole effective mass (m_h^*) variation with temperature for group III-V semiconductors can be found by using the following expression as reported by S. Adachi.[72] The temperature dependence of m_h^* assumes that the hole mass varies with temperature shift of the bandgap (E_g).

$$m_h^*(T) = m_h^*(0)\frac{E_g(T)}{E_g(0)} \tag{3.29}$$

Here $m_h^*(0)$ and $E_g(0)$ are the mass and bandgap values at $T = 0$ K, respectively. The bandgap variation with temperature is taken as $E_g(T) = E_g(0)$ - $\alpha T^2/(\beta + T)$. There are discrepancies among bandgap parameters and several values have been tried out as listed in Table 3.3. The different values could be due to different growth conditions. However, values reported by Pavesi et al.[4] give the best fit for our data. The calculated m_h^* using these data is plotted in Fig. 3.6. It can be seen that Adachi's method gives comparable results to the experimental data. Since, the shape of the curve is mainly depend on the temperature variation of the bandgap of the material, the parameters in $E_g(T)$ equation can be varied to better fit the experimental data. Adachi's method is also tested for electron effective mass (m_h^*) for n-InP data[2] which shows a similar trend. The same trend (effective mass decreasing with increasing temperature) is observed for electrons in n-InP as reported by D. Schneider et al.[2] and for holes in p-InP as reported by K. Hansen et al.[70]

Table 3.3 Values of the parameters for the energy bandgap dependence of InP with temperature. Here, $E_g(T) = E_g(0) - \alpha T^2/(\beta + T)$

$E_g(0)$ (eV)	$\alpha(\times 10^{-3})$ (meV/K)	β (K)	Validity range (K)
[a]1.424±0.005	1.02±3	823±200	0-250
[b]1.432±0.007	0.41±0.03	136±60	77-870
[c]1.4206	0.49	327	0-300
[d]1.4236	0.29	30.63	0-300

[a] Pavesi et al.[4].
[b] Hang et al.[73].
[c] Varshni[3].
[d] Schneider et al.[2]

For semiconductor device designs, an accurate model for the refractive index is crucial, e.g., for determining the optical field distribution in a structure, especially in infrared photodetectors or Quantum Cascade (QC) laser structures. By using the DF model, the wavelength dependent refractive index can be easily calculated. With an increase in doping, the refractive index is reduced with a strong reduction at low photon energies. The calculated refractive index derived from the DF is shown in Fig. 3.7(a) for 1.2 - 24 μm. The refractive index difference (Δn) between doped and undoped samples is shown in Fig. 3.7(c). The refractive index data for undoped InP compared with values obtained from the three term Sellmeier equation[74] in Fig. 3.7(b). This Sellmeier equation can be used to predict refractive index, $n(\lambda)$, in the 1.2 - 13 μm wavelength range as given below,

$$n^2(\lambda) = A + \frac{B_1\lambda^2}{\lambda^2 - C_1^2} + \frac{B_2\lambda^2}{\lambda^2 - C_2^2} \tag{3.30}$$

where the first and second terms correspond to short-wavelength absorption (fundamental bandgap absorption) contributions to the refractive index in the near-infrared region, and the third term denotes the contribution from the far infrared Reststrahlen effect in the mid infrared region. B_1 and B_2 are the strengths and C_1 and C_2 are the approximate wavelengths of the Lorentzian oscillators which represent the absorption mechanisms described above. The Sellmeier coefficients (see Table 3.4) were determined by obtaining least-square fits to the refractive index extracted from the DF as shown in 3.7(b) for comparison. In order to determine A, B_1 and C_1, only the 1.2 - 2.5 μm region is considered, assuming that there is no effect from the third term in this region, since below 2.5 μm the shape of the spectra depends only on the Reststrahlen features in far-IR (28 - 35 μm). A similar assumption is used for undoped and n-doped InP as reported in Ref. [76]. Likewise, B_2 and C_2 were determined using the 2.5 - 13 μm data while keeping previously calculated A, B_1 and C_1 values fixed. The DF is obtained for additional dopings by fit to the experimental absorption coefficients reported in Ref. [55]. The increase in C_1 with doping is due to band gap narrowing, and the decrease in C_2 is due to blue shifting of the plasma frequency due to free carrier absorption. Even though refractive index decreases with doping, beyond 22 μm, the magnitude of n for

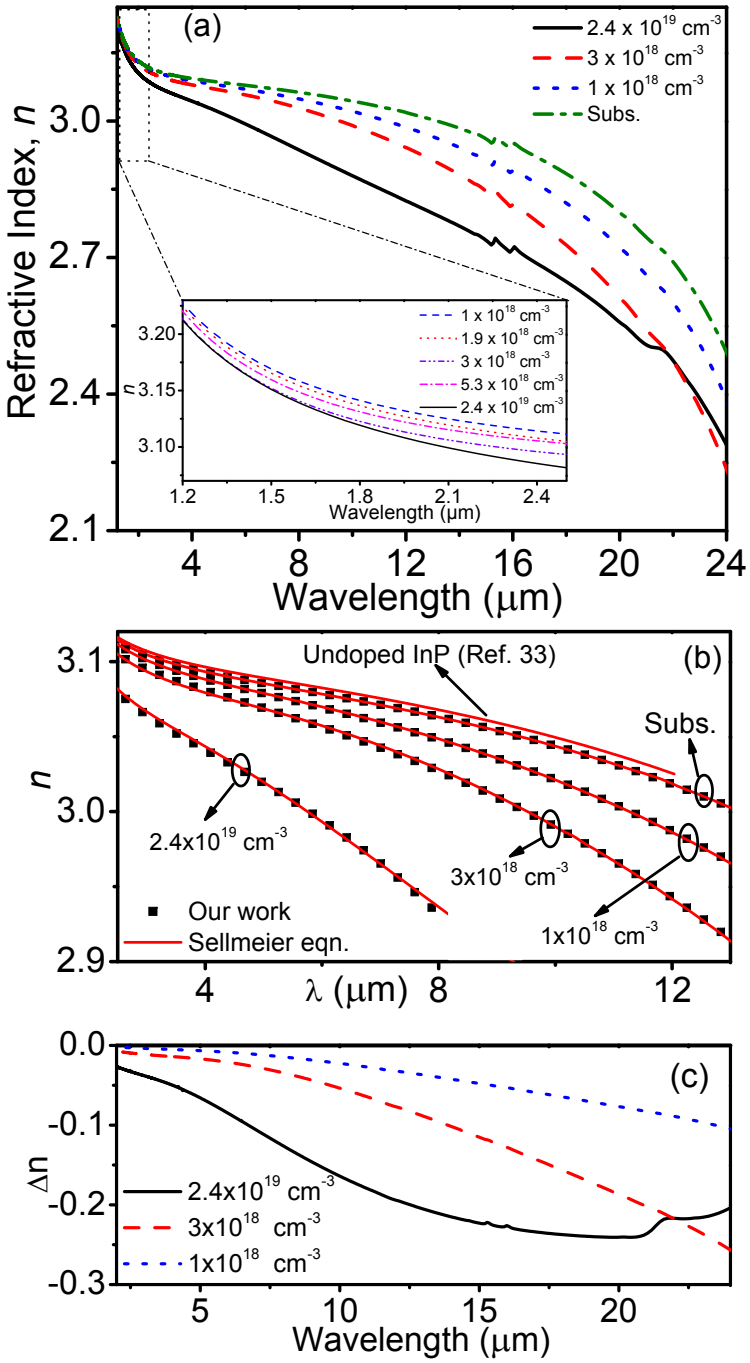

Figure 3.7 Calculated refractive index is shown in (a) for different doping concentrations. The inset in (a) shows an expanded view of the 1.2 - 2.5 μm region for clarity. The least-square fittings made using Eq. 3.30 are shown in (b). In (c), the difference in refractive index (Δn) between the undoped and doped InP is shown. A strong reduction in n in the low-energy region and higher doping samples is the result of increased absorption due to the FC and IVB processes. The highest doped sample shows an increase in n at long wavelengths (> 22 μm).

Table 3.4 Samples used and Sellmeier coefficients (as given in Eq. 3.30) as determined from least-squares fits to the refractive index curves. The first column shows the nominal doping values from Hall measurements at room temperature. A, B_1, and C_1 correspond to the range 1.2 - 2.5 μm, and B_2, C_2 correspond to the 2.5 - 12 μm range (2.5 - 8 μm range for 2.4×10^{19} cm^{-3}). The uncertainty is given in parentheses.

Sample (cm^{-3})	A	B_1	C_1	B_2	C_2
Undoped[a]	7.255	2.316	0.6263	2.765	32.935
Substrate	7.21	2.342	0.6263	2.83	32.45
	(0.01)	(0.008)	(0.0002)	(0.01)	(0.01)
1×10^{18}	7.05	0.6268	4.11	4.11	32.01
	(0.01)	(0.008)	(0.0005)	(0.01)	(0.03)
[b]1.9×10^{18}	6.95	2.53	0.6280		
	(0.01)	(0.01)	(0.0005)		
3×10^{18}	6.91	2.56	0.6310	5.26	31.90
	(0.01)	(0.01)	(0.0005)	(0.01)	(0.03)
[b]5.3×10^{18}	6.71	2.61	0.6361		
	(0.01)	(0.02)	(0.0005)		
[c]6.2×10^{18}	6.62	2.66	0.6403		
2.4×10^{19}	6.56	2.71	0.6453	10.34	30.19
	(0.03)	(0.05)	(0.0005)	(0.08)	(0.09)

[a] Sellmeier coefficients taken from Ref. [74].
[b] Absorption coefficients taken from Ref. [55] to calculate A, B_1 and C_1.
[c] Sellmeier coefficients taken from Ref. [75].

highest doping starts to decrease. With increasing doping, the refractive index is reduced because of strong free-carrier intra-band absorption as a result of the red-shift of the plasma frequency. The phonon absorption features (around 16 and 21.5 μm) are more prominent in the highest doped sample as seen in Fig. 3.7(c). For semiconductor devices, the operating wavelength could be selected in the low absorption region where the index of refraction is similar to that of the undoped materials. However, there are several crucial spectral regions, e.g., the 8 - 14 μm atmospheric window falling in the IVB range, where the refractive index is sensitive to the doping concentrations. Therefore, a proper consideration of the IVB contributions is necessary to determine accurate refractive index, and concurrently is useful in optimum design of related optoelectronic devices. Also, several modern applications, such as wavelength division multiplexing, design of Bragg reflectors or modal calculations, requires an accurate knowledge of InP refractive index in the 1.3 - 1.5 μm range. These results will be useful for InP based opto-electronic device design and characterization, especially for mid-IR photodetectors and quantum cascade lasers.

3.7 Conclusion

In summary, mid and far-IR absorption processes have been investigated in three different p-type InP samples along with an InP substrate. The absorption coefficient and refractive index extracted from the DF will be useful for various applications, including IR split-off band detector designs.[77] One of the atmospheric windows, 8 - 14 μm, is a crucial spectral region that falls into the scope of IVB effects in which the refractive index is sensitive to the doping concentration. Therefore, the corresponding optical constants along with the doping dependence of refractive index will be useful for modeling semiconductor structures. The temperature dependence of ω_p and hole effective mass will also be useful for designing mid- and far-IR group-III Phosphide based detectors and QC lasers operating at or below room temperature.

CHAPTER 4

InGaAsP/InP HETEROJUNCTION DETECTORS BASED ON INTERVALENCE BAND TRANSITIONS

4.1 Introduction

The InGaAsP/InP material system has been widely used in Quantum Well Infrared Photodetectors (QWIPs),[18, 78, 79] light emitting diodes and laser [19] structures. However, intervalence band transitions (IVB) in this material system is not well studied. This study will be beneficial to infrared (IR) detector designing and understanding the additional IVB absorption in phosphide based lasers.

IR detectors in 3 - 5 μm range, based on intervalence band (IVB) hole transitions from the light/heavy hole (lh/hh) bands to the split-off (so) band were recently reported [20] using p-GaAs/AlGaAs heterostructures. High operating temperatures and additional absorption on top free carrier absorption of these devices attracted the applications in the civilian, industrial, medical, astronomy and military sectors. One of the main objective of this work is to use group III-Phosphides to extend the spectral range of these detectors to mid-infrared (MIR) region by varying the materials with different so splitting energies (Δ_{so}), and study the IVB transitions and their dependence on bias and temperature. For instance, InP will allow 2 - 10 μm detection (Δ_{so}(InP) = 0.108 eV). Developing detectors in the 4 - 8 μm range is useful for short-range detection of bright IR sources such as the proximity fuze that is designed to detonate an explosive device. A detailed study [51] on p-InP thin films has shown enhanced absorption in the 2 - 10 μm range, over the free carrier absorption, due to IVB transitions and its dependence on hole concentration other material parameters. Therefore, IVB absorption can be used to enhance the response of group III-Phosphide IR photodetectors.

The Δ_{so} of $In_{1-x}Ga_xAs_yP_{1-y}$ can be tuned for a wide energy range from 110 to 379

meV (11 - 3.3 μm) by changing y from 0 to 1 (Δ_{so} = 0.11 + 0.24y) while still maintaining the lattice matched condition with InP. Therefore, this will allow p-InGaAsP/InP HEIWIP IR detectors to fine tune Δ_{so} in 3.3 - 11 μm range. Also, the free carrier threshold depends on y as $\Delta E_V = 0.502y - 0.152y^2$. Here, ΔE_V is the valence band discontinuity. However, the *so* band should be below the lh/hh band edge of the barrier to avoid carrier trapping in the *so* band. Therefore, free carrier threshold wavelength is typically longer than split-off threshold wavelength.

An InGaAsP/InP heterojunction interfacial work function internal photoemission (HEIWIP) detector (see Fig. 4.2) is used to demonstrate IR response originating from hole transitions between lh/hh bands and the *so* band. HEIWIP detectors consist of alternating highly p-doped absorbing layers (emitters) and undoped barriers. The carriers in the emitters are excited by incoming radiation originate from hole transitions taking place either between different bands (IVB absorption, especially from the *hh* band to the *so* band, or within the same band (free-carrier absorption). These holes then escape over the barriers by a photoemission process occurring at the emitter-barrier interface. The internal work function is defined by energy difference between the barrier bottom and the Fermi level of emitters, and determines the threshold wavelength.

This detector was designed to have free carrier threshold wavelength of 10 μm and split-off threshold of 6.8 μm. In experimental measurements, the detector shows both photovoltaic and photoconductive response with the expected free carrier threshold wavelength at 79 K and intervalence band response in the MIR range. The IVB transitions of InGaAsP are also identified in the spectral response.

4.2 Intervalence band detector mechanism

A detector based on intervalence band transitions has a similar structure as HEIWIPs, described in Sections 1.1 and 2.1. The emitters must be p-doped since the transitions involve are intravalence band. A band diagram ($E-k$) for an emitter region of the detector is shown in Fig. 4.1. In order to explain the detection mechanism, three valence bands will have to

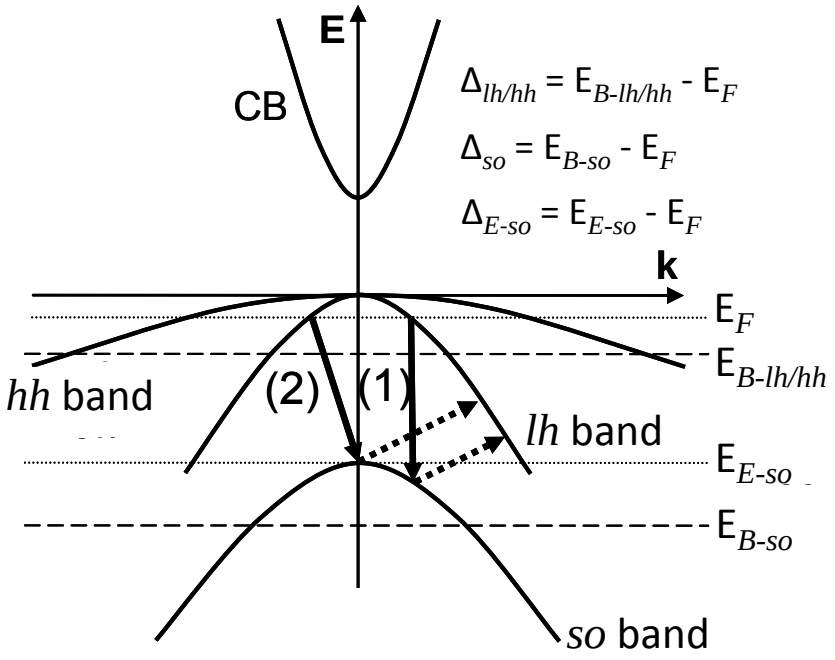

Figure 4.1 A band diagram for an emitter region of the detector, illustrating the different IR detection threshold mechanisms. The horizontal dashed lines $E_{B-lh/hh}$ and E_{B-so} indicate the lh/hh and split-off (so) band maximum (k=0) positions in the barrier. The horizontal dotted lines E_F and E_{E-so} indicate the Fermi energy and the split-off energy in the emitter at k=0. The arrows indicate the possible threshold transition mechanisms (1) direct transition from lh band to so band followed by scatter back to lh band (2) indirect transition followed by scatter back to lh band.

be considered as shown in Fig. 4.1, the light-hole (lh) and heavy-hole (hh) bands which are degenerate at $k = 0$, and the split-off band (so) which is separated from them by an energy E_{E-SO}. Under equilibrium conditions, a p-doped region will have a Fermi level in the lh and hh bands, but above the so band maximum. The arrows in Fig. 4.1 indicate the possible threshold transition mechanisms. These transitions could be direct or indirect. Once the carrier is in the so band, it can escape directly or scatter back into the lh/hh bands and then escape. For a direct transition (shown by arrow 1 solid part) there is no phonon involved, hence k is conserved. The excited carrier then must scatter back to the lh band (or possibly to the hh band although this involves much higher k changes) in order to escape. This phonon involved scattering is shown by the dashed arrow. The threshold for this process is determined by the difference of energy in the light and split-off hole bands at k corresponding to the Fermi energy shown by E_F. For the indirect transition (shown by arrow 2) a phonon is involved and higher energies are possible. The high energy transition which is below the barrier in the split-off band could escape directly (it is not shown as this is a purely spatial change and does not affect the k-space picture). The indirect absorption has two thresholds. For escape with a scattering, it is the difference of the Fermi energy and the split-off band at $k = 0$ in the emitter (Δ_{E-so}). For escape without scattering, it is the difference between the Fermi energy and the so band at $k = 0$ in the barrier (Δ_{so}). The horizontal dashed lines $E_{B-lh/hh}$ and E_{B-so} indicate the lh/hh and so band maximum (at $k = 0$) level in the InP barrier. The horizontal dotted lines E_F and E_{E-so} indicate the Fermi energy and the split-off energy at $k = 0$, respectively. Even though Δ_{so} is constant for a given material system, $\Delta_{ll/hh}$ (also known as free carrier threshold) can be adjusted by varying the In fraction x and the doping concentration of the emitter layer.[14] The value of $\Delta_{ll/hh}$ is the lowest barrier for the excited carriers in the ll/hh bands, and this sets the threshold wavelength for the free carrier mechanism and the major contribution for the dark current, hence determining the maximum operating temperature. By making $\Delta_{ll/hh}$ larger it is possible to make the split-off transitions the dominant detection mechanism and to increase the operating temperature. However, higher $\Delta_{ll/hh}$ can lead to lowering the response by reducing the escape probability

of impact ionizing carriers due to high-energy photons.

4.3 Intervalence band response of an InGaAsP/InP detector designed for mid-infrared

The intervalence response was first demonstrated using GaAs based detectors in the 2 - 15 μm spectral range.[20, 80] This idea is extended to higher absorption in the mid-infrared region by using InGaAsP as the emitter material. The split-off threshold can be varied by changing the As alloy fraction of InGaAsP material.

The detector consists of 10 periods of p-doped 30 nm thick $In_{0.86}Ga_{0.14}As_{0.3}P_{0.7}$ emitters doped to 3×10^{18} cm^{-3} and 65 nm thick InP barriers as shown in Fig. 4.2. The alloy fractions were chosen to lattice match InGaAsP to InP. The top and bottom contacts were 1×10^{19} cm^{-3} p-doped $In_{0.53}Ga_{0.47}As$ layers with 0.15 and 0.7 μm thickness, respectively. These InGaAs layers were implemented to have good ohmic contacts with the metal wire bonds and were latticed matched to InGaAsP layers. The adjacent InGaAsP layers to the InGaAs layers were grown thicker (40 nm) than the other InGaAsP layers to compensate the depletion region due to biasing of the structure. The energy band diagram (calculated using nextnano - semiconductor software) of the detector structure is shown in Fig. 4.3 for zero electric field for the first four layers. The main IVB transitions along with their energy values are also shown. These transitions are also shown in the responsivity spectra (see Fig. 4.4). Spectral response was measured on devices with an optical active area of 260 $\times$ 260 μm^2 by using a Perkin-Elmer System 2000 Fourier Transform IR (FTIR) spectrometer. A bolometer with known sensitivity is used for background measurements and calibrating the responsivity of the detector. The photoconductive response is shown in Fig. 4.4. As shown in Fig. 4.3 and Fig. 4.4, the transition with 120 meV (10.2 μm) is the lowest threshold of the detector originating from free carrier absorption in the same lh/hh bands. The transitions with 224 meV (5.5 μm) corresponds to InGaAsP split-off threshold. Ideally, the IVB transitions in InGaAs should correspond to 295 meV (4.2 μm). However, due to a sharp interface edge formed by band discontinuity, it could give two thresholds as can be seen in the

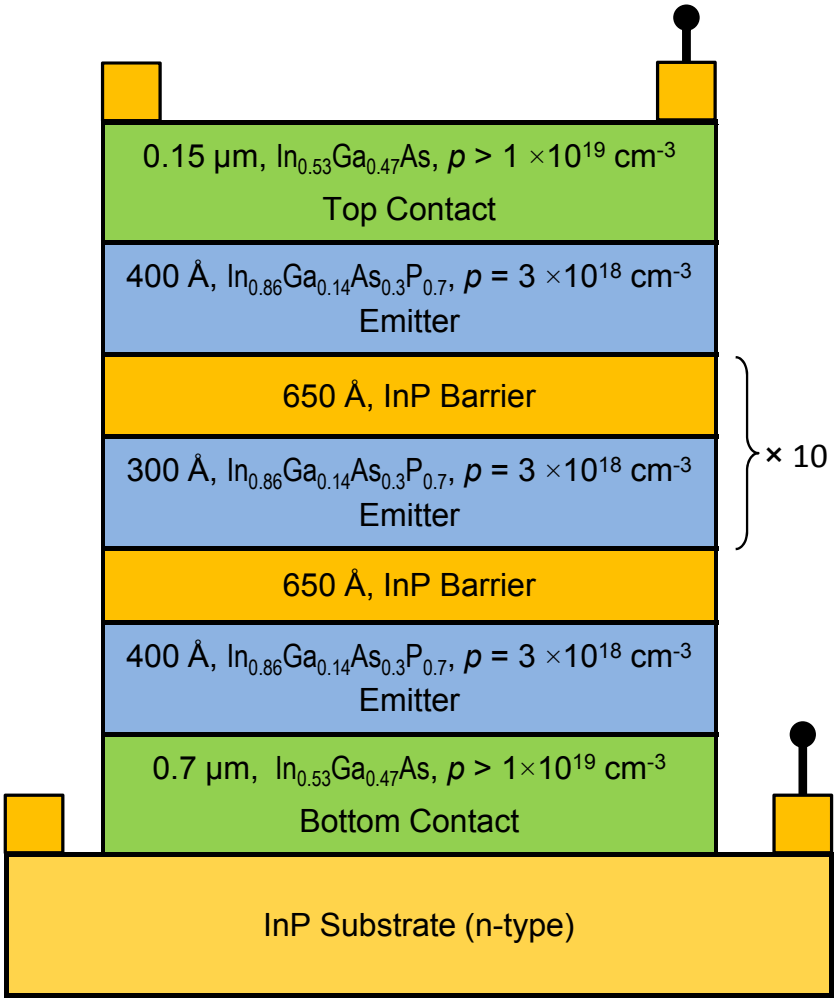

Figure 4.2 Detector structure of InGaAsP/InP detector. The number of emitter/barrier periods, emitter and barrier thickness, and doping values are given.

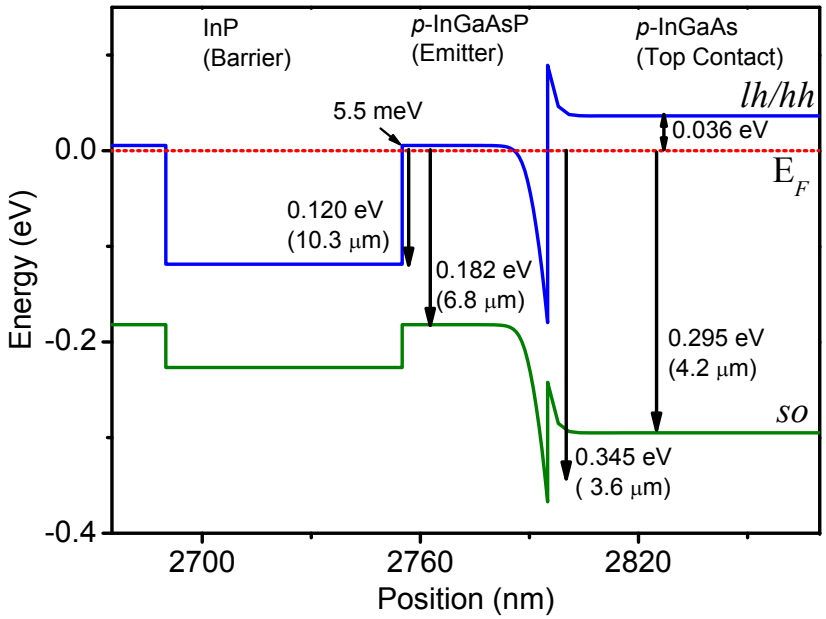

Figure 4.3 Energy band diagram of InGaAsP/InP detector for the first four layers of the structure. The arrows show the work function in meV for different hole transitions and the corresponding threshold wavelength in parenthesis.

shoulders of responsivity curves at 345 meV (3.6 μm) and 264 meV (4.7 μm). In the inset of Fig. 4.4, the E-k diagram (taken from Fig. 4.1) for the emitter is shown with possible IVB transitions. The number in the parenthesis for the arrows showing the shoulders of the spectral peaks indicate if the transition is direct(1) or indirect(2). It seems that most of the IVB transitions are indirect. The spectral response ($>$ 3.5 μm) due to InGaAsP IVB transitions increases with increasing bias while that of InGaAs has the opposite effect. Therefore, responsivity (in MIR range) due to IVB transitions can be enhanced by increasing the electric field. Generally, the photoemission process determines the escape rate of holes out of the emitter region following an escape cone model.[16] However, with increasing bias, the thermal assisted tunneling contribution will mix in this process deteriorating the model accuracy, which can be seen from the increasing threshold wavelength with bias. The increase in response with temperature may be related to phonon effects on the escape rate for excited carriers. As the temperature was further increased, the responsivity decreased, and was not measurable beyond 190 K. A peak response of 4.5 V/W at 2.3 μm and 0.4 V/W at 4.5 μm was seen at 79 K for photovoltaic mode. Photovoltaic response of this detector is three times higher at 4.5 μm and 79 K when compared to a similar GaAs/AlGaAs split-off detector [44] which was designed to have same threshold wavelength. Also, this detector has stronger near-IR response due to interband and split-off absorption of the InGaAs layer. Therefore, InGaAsP/InP material system is better than GaAs based system for both NIR and MIR applications.

Detectivity (D*) was calculated (see Appendix A for details) using the measured noise current density with the sample mounted in an optically and electrically shielded dewar. The primary noise sources are believed to be the generation recombination and Johnson noise. D* was obtained using the formula $D^* = (R \times \sqrt{A})/I_N$, where R is the responsivity in A/W, A is the optically active area of the detector (in cm^2) and I_N is the noise current density (in A Hz$^{-1/2}$). The calculated D* is 2.5 $\times 10^5$ Jones at 2.3 μm and 1.8 $\times 10^4$ Jones at 4.5 μm for 79 K for photovoltaic response. The low responsivity and detectivity of the InGaAsP/InP detector compared to GaAs/AlGaAs detector could be due to the smaller

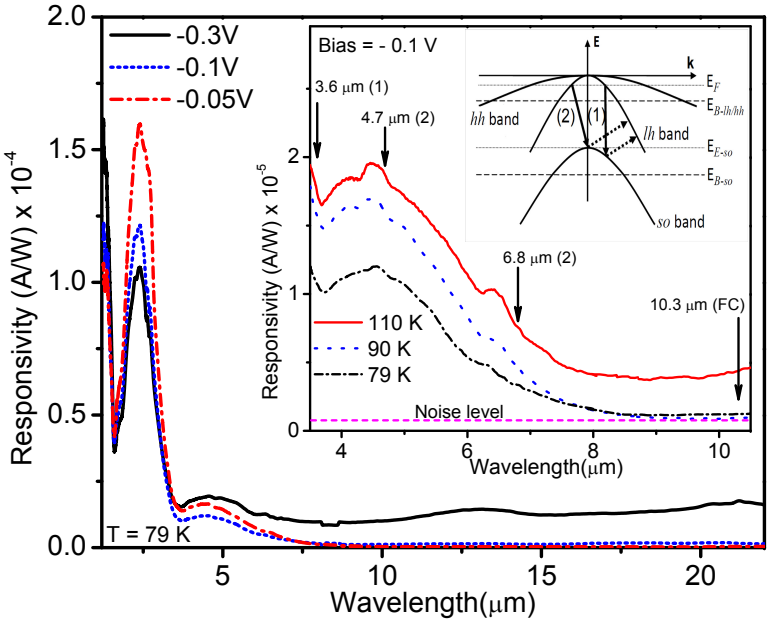

Figure 4.4 Measured spectral response of InGaAsP/InP detector for different bias values at 79 K. The inset shows responsivity for different temperatures under -0.1 V. The arrows show the shoulders of the peaks corresponding to different energy transitions depicted from the energy band diagram in Fig. 4.3. In addition, E-k diagram for the emitter is shown with possible IVB transitions. The number in the parenthesis for the arrows showing the shoulders of the spectral peaks indicate if the transition is direct(1) or indirect(2). FC denotes the free carrier absorption.

number of emitter/barrier periods in the structure. This will also cause low total impedance inside the structure. Therefore, the detectivity can be further improved by increasing the number of emitter/barrier periods.

Furthermore, dark current at different temperatures was measured to produce Arrhenius plots which are used to calculate work function (threshold wavelength) of the detector. The dark current was measured using 4-terminal sensing technique to correct for the wire resistance as the device operates at low bias voltages. Here, the device resistance is close to 1 kΩ at 80 K. Because, the typical 2-terminal current-voltage measurements introduce bias errors in the measurements. This is due to the high potential drop across the wires compared to the actual bias applied across the device at low bias values, which leads to measuring an incorrect voltage across the device. The Arrhenius plots based on dark current measurements are shown in Fig. 4.6(a). The linear region selected for Arrhenius calculations is 80 - 130 K. The work function (Δ) obtained from the slope is 51.9 meV for 0.1 V bias. This gives a threshold wavelength of 23.9 μm. This threshold is longer than the one seen on spectral response. Under low-bias operation (electric field $<$ 1 kV/cm), the thermionic current is coincident with Ohms law and the image-force effect on the thermal activation energy. This makes thermionic current linearly proportional [81] to bias, hence R_0A product can be defined as $R_0A = [(\partial J_{TE}/\partial V)^{-1}]_{v=0}$, where A is the mesa area of the device and R_0 is the device resistance at zero bias. This formula implicitly includes a term $\exp[\Delta/k_BT]$. Therefore, slope of $\ln(R_0A)$ vs. $1/T$ can be used to extract Δ as shown in Fig. 4.6(b). Two linear regions have been identified in these plots: slope 1 (Δ_1 = 63.9 meV) for T = 80 - 110 K and slope 2 (Δ_2 = 105.8 meV) for T = 120 - 140 K. The threshold wavelengths corresponding to these work functions are 19.3 μm and 11.7 μm. It seems that even though Δ_1 is similar to the value got from Arrhenius data, for higher temperature range the calculated threshold becomes closer to spectral threshold. This indicates that thermionic emission is more dominant at high temperatures making Arrhenius plots more accurate.

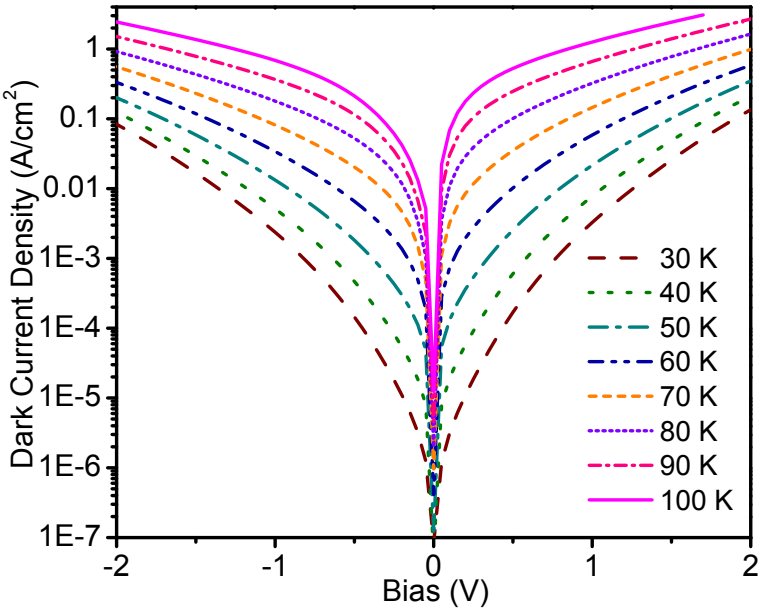

Figure 4.5 The dark current density for the InGaAsP/InP detector measured at 30 - 100 K showing thermionic emission. These data were used to calculate Arrhenius plots.

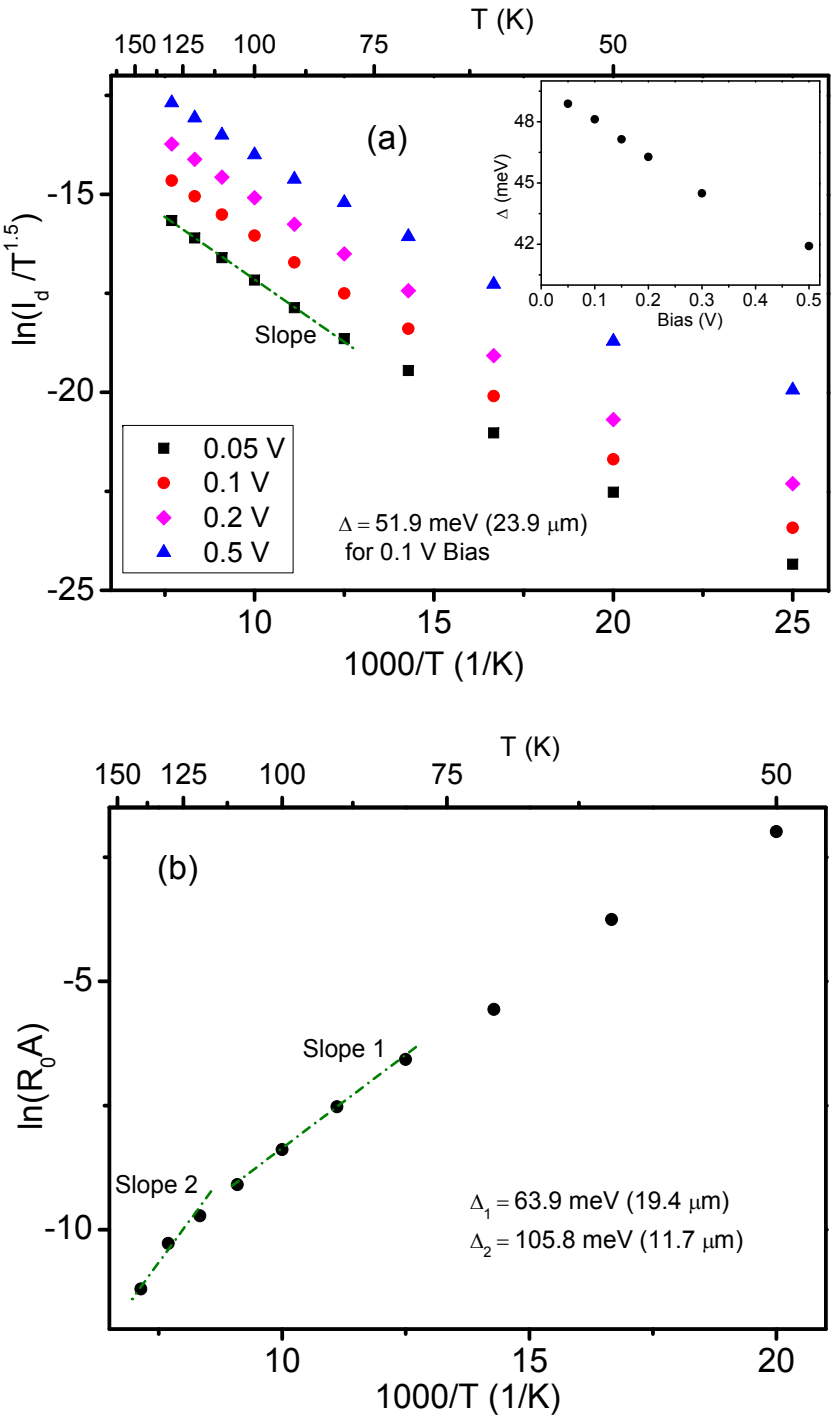

Figure 4.6 (a) Arrhenius plots for different bias values are shown. Here, I_d is the dark current. The inset shows the work function change with bias. (b) Temperature dependence of R_0A is shown (R_0 = device dynamic resistance at zero bias). Two different linear regions have been identified with work functions Δ_1 = 63.9 meV (for T = 80 - 110 K) and Δ_2 = 105.8 meV (for T = 120 - 140 K). The corresponding threshold wavelengths are 19.4 μm and 11.7 μm, respectively.

4.4 Further Improvements

The responsivity of the detector can be further improved by increasing the number of emitter/barrier periods.[77] For instance, the responsivity can be increased by a factor of ∼3 by increasing the number of periods from 10 to 30. This will also increase the device impedance. In addition, surface plasmon effects can be implemented to enhance the absorption in the top surface and improve D^* by a factor of ∼15 according to theoretical models.[82, 83] The photovoltaic mode operation of this device will have lower dark current and hence better D^*. The photovoltaic response of this detector could be due to a slight gradient in the barriers which occurred from growth process. The results shown in this work are not from a device designed for optimized photovoltaic mode operation. As described for similar GaAs/AlGaAs photovoltaic detector structures [43], a graded barrier can be used in place of the flat barrier to improve D^* by a factor of ∼3. Therefore, this photovoltaic operation can be further improved by intentionally making the barriers graded.

4.5 Conclusion

In summary, InGaAsP/InP material system was studied using heterojunction IR detector to better understand the IVB transitions and their bias and temperature dependence. The response of the detector is primarily from heavy/light hole to split-off transitions and free carrier absorption. The detector showed D^* is 2.5 $\times 10^5$ Jones at 2.3 μm and 1.8 $\times 10^4$ Jones at 4.5 μm for 79 K for photovoltaic response. The split-off threshold wavelength of the detector can be varied from 3.5 - 11.2 μm by changing the As fraction of InGaAsP emitters. The response can be optimized by using a graded barrier that reduces trapping and increases the gain. Materials other than InGaAsP may help to extend the coverage to longer wavelengths. Possible materials such as GaN may be able to operate at 60 μm or beyond at elevated temperatures.

CHAPTER 5

HIGH EFFICIENT ANTIREFLECTION COATINGS FOR MULTI-BAND PHOTODETECTORS

5.1 Introduction

In semiconductor detectors, there is significant amount of reflection from the top surface (up to 30% depending on the refractive index of the medium and the wavelength range). This will reduce the light throughput to the detector and also the field of view (more reflection at oblique angles of incidence). Therefore, a properly designed antireflection (AR) coating will reduce this unwanted reflection to a minimum even at higher oblique angles of incidence ($< 60^{\circ}$). In this chapter, I discuss an approach[84] using nanorod multilayer structures for AR coatings, which can be grown on the top surface of the photodetectors. The TiO_2 or SiO_2 nanorod based multilayer structures are expected to reduce reflection in UV to infrared wavelength regions, even at an oblique angle of incident. Shubert et al.[17] have used TiO_2 and SiO_2 graded-index nanorods deposited by oblique angle deposition, and they demonstrate the potential of these antireflection coatings that virtually eliminate Fresnel reflection from an AlN surface over the UV band. This was achieved by controlling the refractive index of the TiO_2 and SiO_2 nanorod layers down to a minimum value of $n = 1.05$, the lowest value so far reported.[17] Conventional single-layer AR coatings work only at a single wavelength and at normal incidence. However, graded-index coatings yield omnidirectional, broadband AR characteristics. Current anti-reflection coatings suffer from transmission losses over a broad field-of-view. As the light source moves from being directly in front of the optical system to off to the side of the optical system, the coating spectral properties tend to blue shift. The use of graded-index coatings with different index profiles for broadband antireflection properties, with air as the ambient medium, is one of the best approaches to reduce reflection and increase transmission throughput. Due to the unavailability of optical materials with

very low refractive indices that closely match the refractive index of air, typical broadband antireflection coatings are not feasible. However, recent developments[17, 85, 86] in growth of TiO_2 and SiO_2 nanostructures deposited by oblique angle deposition have shown very low refractive indices close to that of air. These are potentially good broadband antireflection coatings that virtually eliminate high reflection from the air-substrate interface over a broad range of wavelengths. This is achieved by controlling the refractive index (n) of the TiO_2 and SiO_2 nanorod layers, down to a minimum value for the layer closest to the air interface and then increasing for other layers. Here I present a comparative study of the performance of multi-layer structures having different number of layers , and I demonstrate the requirements for effective AR coatings.

The proposed AR coatings will also be useful for enhancing the quantum efficiencies of solar cells and eliminating the need for tracking the moving Sun. Another application is improving the reflectance of Bragg Reflectors by increasing the difference of refractive indices between two media. The proposed strategy to reach the goal of identifying a structure with better uniformity, better performance and wider coverage over a broad visible (VIS) range, is to use graded index multi-layer coatings. Fabry-Perot oscillations can be minimized by varying the layer thickness and refractive index. It is envisioned that the nanostructured technology can be utilized in optical sighting systems to decrease both the off-angle reflections and overall optical system sizes.

5.2 TiO_2 nanostructured samples and experimental techniques

Titanium dioxide (TiO_2) has gained extensive interest for its important role in many applications, such as catalyst, photocatalyst,[87] gas sensor,[88] and optical and optoelectrical devices.[89] Using an oblique angle deposition technique, an array of well-aligned and tilted TiO_2 nanorods has been fabricated by an electron-beam evaporation method on glass and Silicon substrates. This technique allows for highly directional vapor flux and can be implemented with a variety of materials needed for growth of oblique angle nanorods. More details of the growth process can be found in Ref. [85]. TiO_2 films exhibit a slanted column

growth. The inter-columnar pore is opened and increases with the increase of flux angle. Nanorod angle is defined as the angle between substrate surface normal and the long axis of slanted nanorods, and it is a significant structural parameter. It can be seen that the columns incline towards the direction of the incoming flux. The nanorod angle increases with the increase of flux angle. The porosity of the nanostructured layer increases with the flux angle and consequently decreases the effective refractive index of the medium. Transmittance and reflectance spectra were measured to characterize these TiO_2 nanostructured thin films using Ocean Optics USB4000 spectrophotometer in visible range and Perkin-Elmer System 2000 FTIR in infrared region.

5.3 Theoretical Model

The intensity-transfer-matrix method[62, 90] was used to calculate reflectance and transmittance spectra from the three phase vacuum/film/substrate multilayer structure. The interface matrix ($Q_{j\text{-}1,\,j}$) which represents the interaction of light between the $(j-1)^{th}$ and j^{th} layers is given by

$$Q_{j-1,j} = \frac{1}{2}\begin{bmatrix} 1+q_{j-1,j} & 1-q_{j-1,j} \\ 1-q_{j-1,j} & 1+q_{j-1,j} \end{bmatrix}. \tag{5.1}$$

Where, $q_{j-1,j} = \sqrt{\epsilon_j}\cos(\theta_j)/\sqrt{\epsilon_{j-1}}\cos(\theta_{j-1})$ for s-polarized and $q_{j-1,j} = \sqrt{\epsilon_{j-1}}\cos(\theta_j)/\sqrt{\epsilon_j}\cos(\theta_{j-1})$ for p-polarized light and $\sqrt{\epsilon_j}$ is the dielectric function of the j^{th} layer.

The propagation matrix (P_j) for the light propagation in the j^{th} layer with thickness d_j is described by

$$P_j = \begin{bmatrix} \exp(i2\pi\sqrt{\epsilon_j}d_j\cos(\theta_j)/\lambda) & 0 \\ 0 & \exp(-i2\pi\sqrt{\epsilon_j}d_j\cos(\theta_j)/\lambda) \end{bmatrix}. \tag{5.2}$$

The refracted angle in the j^{th} layer is obtained from Snell's law, $\theta_j = \sin^{-1}[\sqrt{\epsilon_{j-1}}\sin(\theta_{j-1})/\sqrt{\epsilon_j}]$.

The total transfer-matrix, M, is the multiplication of the matrix in layer 0 through layer N ($j = 0$ representing the light incoming media), i.e., $M = \prod_{j-1}^{N} P_j Q_{j-1,j}$. The reflectance

(R) and transmittance (T) are expressed by

$$R = \left|\frac{M_{21}}{M_{11}}\right|^2 \text{ and T} = \frac{\text{Re}(\sqrt{\epsilon_{\text{N}}})}{\text{Re}(\sqrt{\epsilon_0})}\left|\frac{\text{det(M)}}{\text{M}_{11}}\right|^2. \tag{5.3}$$

The multiple reflected beams from the substrate surfaces are added incoherently to neglect the phase information as described in Ref. [63].

5.4 Results and Discussion

Single layer TiO_2 nanorods grown on both glass and undoped Si substrates were studied for their refractive index variation with their deposition angle. The highly orientated nanostructure of the slanted nanorods indicates that these films are anisotropic,[91] with the long axis parallel to the nanorod growth direction. The anisotropic structure will introduce the anisotropic dependence into the thermal, electrical, magnetic and optical properties of thin films.[92] The bundling behavior of the slanted columns is observed at higher flux angle of TiO_2 films, which is the result of the anisotropic shadowing effect.[93] The nanorod angle increases with the increase of vapor flux angle.

5.4.1 Single layer TiO_2 nanorods on glass

The transmittance spectra of TiO_2 films on glass substrate are shown in Fig. 5.1(a). The transmission decreases with increase of flux incident angle (ϕ_f). The nominal thickness of the thin films is 2 μm. Due to the interference of the incident light, constructive wave interference and destructive wave interference occur periodically. This known as Fabry-Perot (FP) oscillations. Therefore, the transmittance spectra of TiO_2 films exhibited many peaks and valleys. It can be seen that transmittance increases with the increase of growth flux angle. The effective refractive indices of TiO_2 films were extracted by matching calculated transmission spectra with experimental values using the methods described below.

In order to find the complex refractive index of the nanorod thin film, the intensity-transfer-matrix was used to calculate the transmission of the thin film-substrate structure.

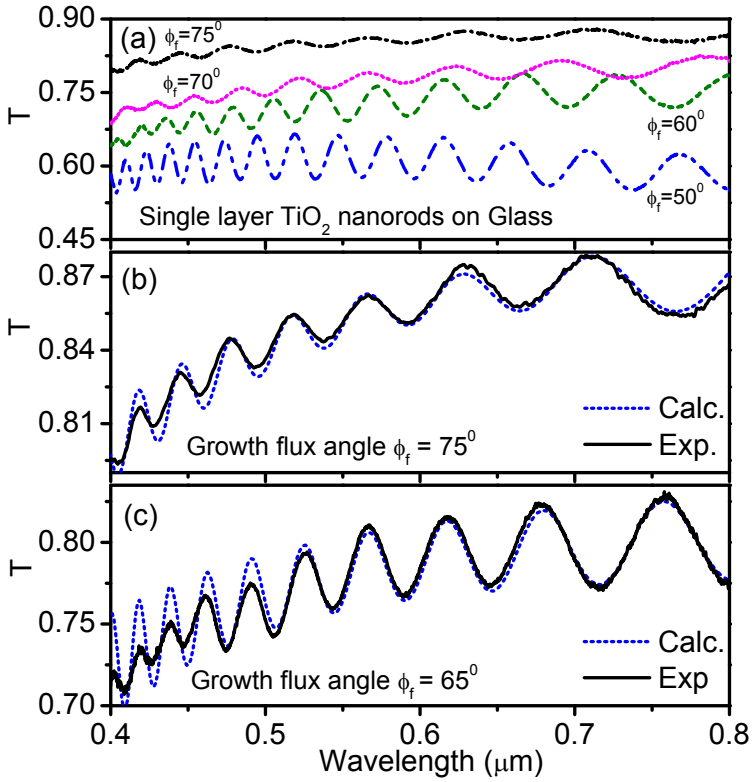

Figure 5.1 (a) Transmittance spectra of single layer TiO_2 nanorod films deposited at different flux angles. The transmission increases with an increase of deposition angle. Comparison of experimental transmission data with calculations for (b) 75° and (c) 65° growth flux angles on glass substrate.

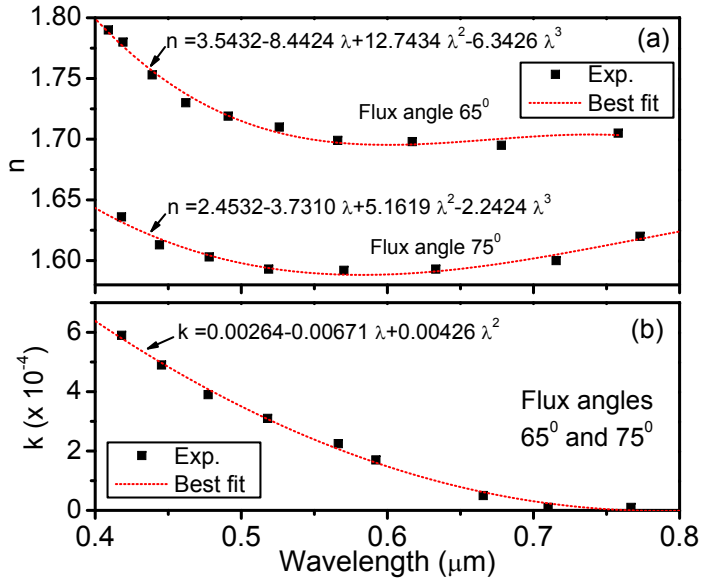

Figure 5.2 (a) Real and (b) imaginary parts of the refractive index determined by matching the FP peaks at different wavelengths. The squares represent the value at each FP peak. The best fit curve was used to find the values at intermediate wavelengths. The imaginary part is the same for both the samples.

In the fitting procedure, first the real part of the refractive index is interpolated from the values reported in Ref. [17]. Then the thickness of the nanorod layer was varied around the nominal thickness of the layer (2 μm) until an approximate fit to the FP peaks is observed. Next, the real part of the refractive index is varied slightly to match better the FP peaks with the experimental data. These fitting results are shown in Figs. 5.1 (b) and 5.1(c) for different flux angles. The low amplitudes of the FP peaks in the experimental spectra could be due to the light scattering in the shorter wavelength region. The extracted real part of the refractive index values are plotted in Fig. 5.2(a) along with the best fit line. The effective refractive index of TiO_2 films decreases with the increase of flux incident angle. The attenuation effect in transmission spectra is due to the imaginary part of the complex refractive index. The value of this was found by matching the average height of the FP peaks with the experimental data. These values are plotted in Fig. 5.2(b). Both 65° and 75° samples have the same attenuation. The absorption in the layers calculated from imaginary part of the refractive index is less than 0.15 % over a wavelength range from 0.4 - 0.9 μm.

5.4.2 Single layer TiO_2 nanorods on Silicon

The same growth technique was used to grow TiO_2 nanorods on undoped Si substrate as described above. In this case, the refractive index of the substrate is larger than that of nanorod thin film layer. Therefore the reflection from the air/TiO_2 nanorod interface should be less than that of air/Si interface. In other words, the TiO_2 nanorod layer can act as an AR coating for Si surface. This is confirmed by the measured reflection spectra for different samples as shown in Fig. 5.3. The strong FP oscillations are characteristic of nanorod layer thickness and the refractive index of the medium. Comparison of experimental reflectance data with calculations for a single TiO_2 nanorod film deposited at 75° flux angle on a Si substrate is shown in Fig. 5.4. The *s*-polarized component of the reflectance increases with increasing incident angle while the *p*-polarized component decreases. Only the real part of the refractive index is used to simulate reflectance data. The refractive index is found to be the same for all the incident angles displayed in Fig. 5.4.

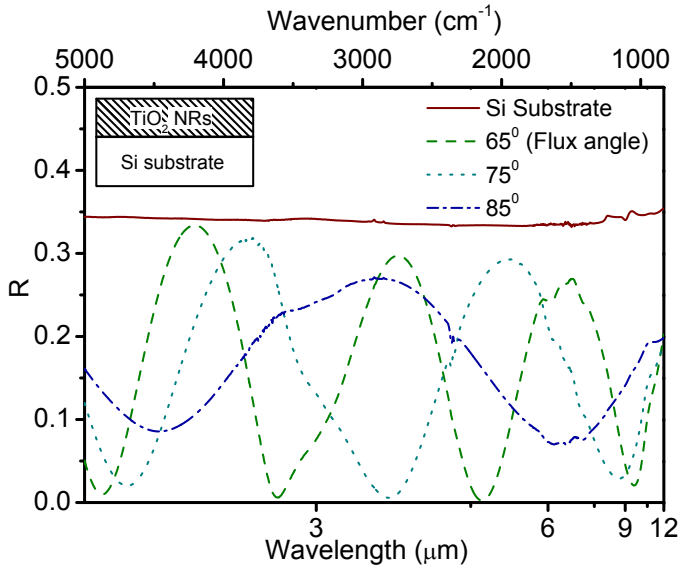

Figure 5.3 Measured reflectance spectra at near normal incidence for nanorod layers grown on Si substrate at different growth flux angles. The wavelength axis is a reciprocal scale of wavenumber axis.

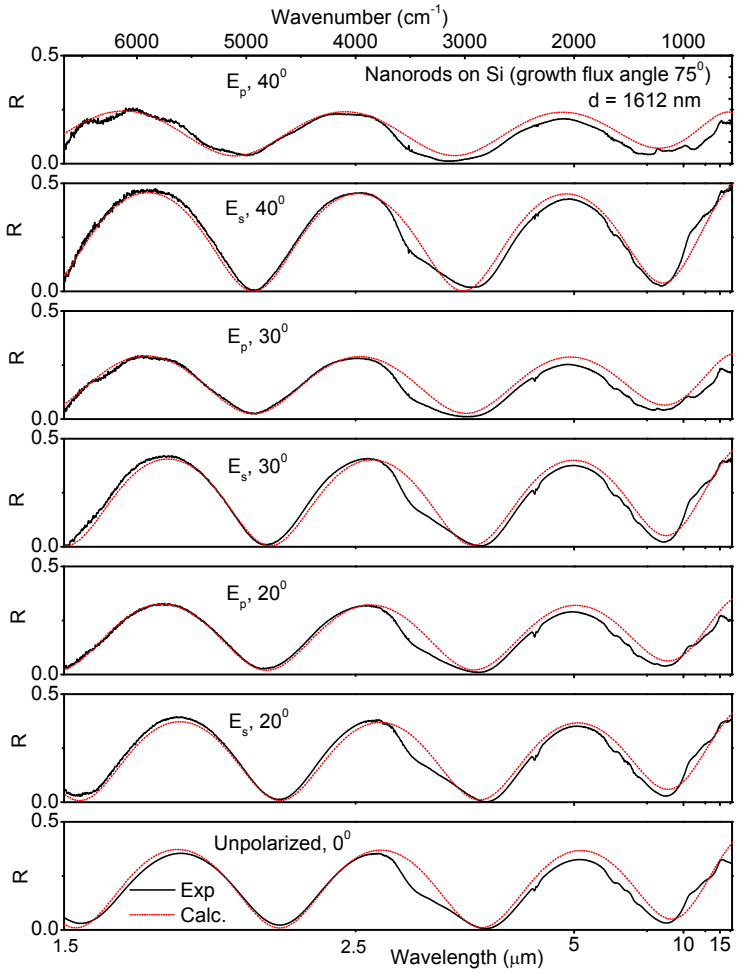

Figure 5.4 Comparison of experimental reflection spectra with calculations for a single layer TiO_2 nanorod film deposited at 75° flux angle on a Si substrate. Here, the *s*-polarized component (E_s) increases with increasing incident angle while *p*-polarized component (E_p) decreases.

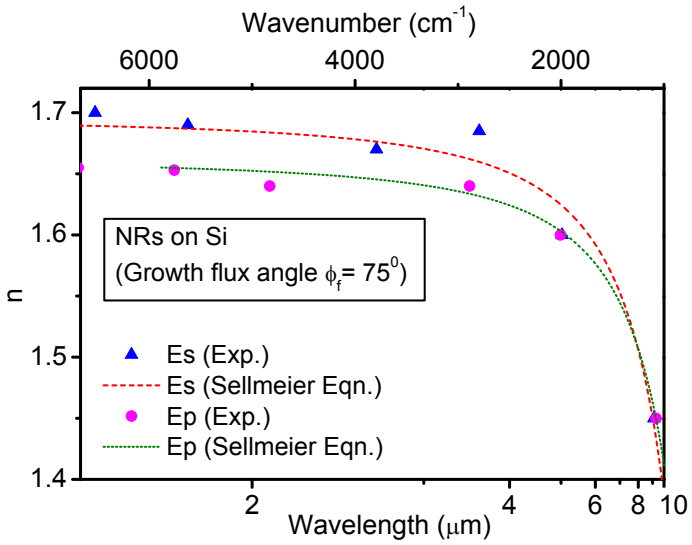

Figure 5.5 Calculated refractive index of nanorods (NRs) grown on Si substrate for *s*- and *p*-polarized light is shown. The dots and triangles represent the values found at FP peak positions. The dotted and dashed lines show the corresponding Sellmeier equation obtained by least squares fitting.

These values of the scattered refractive index were then fitted by the two term Sellmeier dispersion equation given below. This equation has the same form as given for a TiO_2 bulk crystal,[94]

$$n^2(\lambda) = A + \frac{B\lambda^2}{\lambda^2 - C^2} \ . \tag{5.4}$$

The calculated refractive index for s and p polarized light is shown in Fig. 5.5. The dots and triangles represent the values found at FP peak positions. The dotted and dashed lines correspond to the Sellmeier equation obtained by least square fitting. The Sellmeier coefficients are listed in Table 5.1 for polarized light.

5.5 Optical Characterization of Multilayer AR Coatings

In this section, the feasibility of a numerical design of multilayer AR coatings on group III-V (such as GaN,[15, 31]) based mid-infrared detectors is discussed. The multi-layers can be grown from above mentioned nanorod structures. The utility of AR coating designs found in this study will depend on the width of the spectral region (2 - 12 μm) over which they are effective. Typically, a single homogeneous layer of refractive index n will reduce to zero the normal-incidence reflectance of an interface between a substrate of refractive index n_s and a medium of refractive index n_m for light of wavelength λ provided that its optical thickness (d_{opt}) is equal to $\lambda/4$ and the refractive indices satisfy the relation $n = \sqrt{n_s n_m}$. Through use of multiple thin layers, it is possible to obtain zero reflectance at one or more wavelengths even if the refractive-index relationship given above is not satisfied. The main objective of this study is to find out the effect of number of layers and their refractive indices on the reflection of the AR coating. The intensity-transfer-matrix method is used to calculate reflection spectra assuming constant refractive index for the nanostructured medium. In theory, infinite number of layers with a graded refractive index profile will reduce the interface reflection to near zero. However, fifteen layers with quarter-wave d_{opt} is generally more than adequate.[95] For a discrete layer model, interference effects take

Table 5.1 Sellmeier coefficients for s- and p-polarized light (from Eq. 5.4) as determined from a least-squares fit to the experimental refractive index data points as shown in Fig. 5.5. The tolerance is given in the parentheses.

	A	B	C
E_s	2.876(0.002)	77.01(0.05)	90.42(0.05)
E_p	2.754(0.002)	77.27(0.05)	101.49(0.05)

place at the abrupt interfaces between the individual layers. This will introduce Fabry-Perot interference from the multilayer structure. This plays a major role in light transmitted at particular wavelengths. In other words, depending on the thickness and refractive index of the layers, the overall reflection and transmission will get increased or reduced at certain wavelengths due to constructive and destructive interference from multiple reflections. It is possible to fine tune the thickness of each layer and the number of layers to minimize the overall reflection by enhancing destructive interference in the multilayer structure. The optimization process is discussed in the following part of this section (the important steps of the program used for this calculation are shown in Appendix C).

A refractive-index profile of a 15-layer stack grown on GaN substrate is considered for simulation of an AR coating for a n = 1.00 - 2.3 interface. Here, the refractive index [96] of GaN is taken as 2.3 for the given infrared region. The refractive indices of adjacent layers in this system differ from one another by 0.1 (except first and last two layers) as depicted in the inset of Fig. 5.6. All the sublayers have the thickness of d_{opt} = 0.4 μm for normal incidence. The total thickness of the AR coating is 6 μm. Note that d_{opt} depends on the angle of incidence of incoming light. First, the average reflectance for s- and p-polarized light of this system was calculated as a function of angle for light for the broad spectral region 2 - 12 μm. The above mentioned d_{opt} was chosen by reducing the overall reflection from the multilayer stack. Additional calculations have shown that an increase and decrease in the value of the d_{opt} from the one cited above resulted in a deterioration of the performance. At longer wavelengths the deterioration increases, because the optical thickness will approach a half-wave and then the layers will become absentee layers. At shorter wavelengths the overall thickness of the structure will no longer be large enough, hence the performance is deteriorated. Also, the performance is degraded or improved when the refractive index difference between adjacent layers is increased or decreased because this impacts on the accuracy of the approximation of the inhomogeneous layer. The average reflectance of s- and p-polarized light at different angles is shown in Fig. 5.6. The average reflectance remains less than 1.2 % for normal incidence compared to $>$ 16 % without the

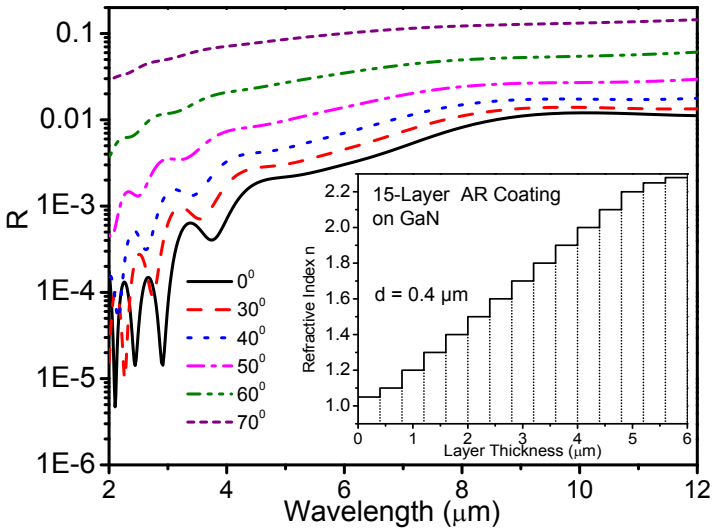

Figure 5.6 The reflection from 15-layer AR coating structures (on GaN substrate) at different angles of incidence. For clarity, the curves for incident angles of 10° and 20° are not shown as they are very close to the curves for 0°. As shown in the inset, the AR coating has a graded refractive index (n) profile from air to GaN ($n_{GaN} = 2.3$) with each layer having a thickness (d) of 0.4 μm. The reflection is below 5.5% for broad wavelength range 2 - 12 μm even at 60°.

coating. Also, reflectance is less than 5.5 % even at 60° across the whole 2 - 12 μm spectral region.

Next, the 15-layer stack is truncated so that it forms a 5-layer AR coating. In designing this structure, the initial layer parameters were obtained from a similar 5-layer stack[17] grown on AlN substrate which was optimized using a quintic refractive index profile[95] in the visible spectral region. However, these layer parameters needed to be modified for the infrared region of our interest. Beginning with the first layer, the index of each layer is then separately adjusted to minimize the broad reflectivity. After individual layer optimization, the new index is retained for use with subsequent layer optimizations. After the last layer, the process is repeated starting again with the first layer until the overall reflectance converge to a minimum. The same process is then carried out to optimize the refractive index for each layer. These two processes can be repeated to optimize the layer parameters by minimizing the overall reflectance of the AR coating.

The index distribution profile and corresponding average reflectance of *s*- and *p*-polarized light at different angles of incidence is shown Fig. 5.7. The average reflectance remains less than 3.3 % for normal incidence for 2 - 8 μm spectral range. Also, reflectance is less than 10.5 % even at 60° for the same spectral range. It can be seen from Fig. 5.7 that the average reflectance of the resulting system is similar to that of Fig. 5.7 considering the advantage of having less number of layers. For a somewhat narrower spectral region, a better solution for the same overall coating thickness or, preferably, a thinner solution of like performance can be obtained. In fact, it should be possible to further reduce the overall thickness and the number of layers by further refinement. Also, other methods such as genetic algorithms[97, 98] could be useful to get better AR coating designs.

The implementation of multilayer AR coatings having low refractive index layers is possible with TiO_2 and SiO_2 nanorod structures. It has been reported[17] that the refractive index of a TiO_2 nanorod layer can be controllably varied from 2.7 to 1.3 by changing the vapor incident angle. The refractive index of a SiO_2 nanorod layer can be varied from 1.46 to 1.05. Therefore a combination of TiO_2 and SiO_2 nanorod layers can easily be used to

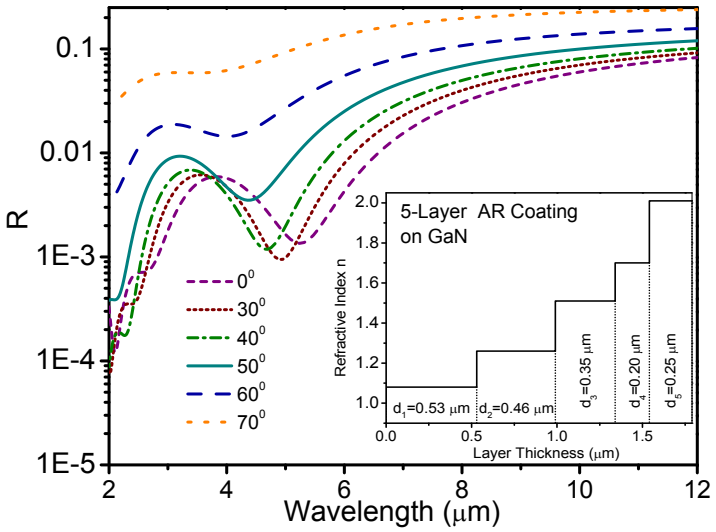

Figure 5.7 The reflection from 5-layer AR coating structures (on GaN substrate) at different angles of incidence. For clarity, the curves for incident angles of 10° and 20° are not shown as they are very close to the curves for 0°. The inset shows the graded refractive index (n) profile of the AR coating from air to GaN ($n_{GaN} = 2.3$) with thickness (d_i) of each layer. The reflection is below 6% for broad wavelength range 2 - 10 μm at normal incidence and below 13% even at 60°.

grow the designed multilayer AR coating.

5.6 Conclusion

It has been shown that, multilayer AR coatings having a graded refractive index profile can be used to obtain very low reflectance even at oblique angles of incidence over a broad spectral range. The feasibility of these AR coatings is made possible by recent developments in low-refractive index TiO_2 and SiO_2 nanostructured material. In this work an optical characterization of TiO_2 nanorods grown on glass and Si substrate was performed to better understand the effective refractive index of single layer TiO_2 nanorod structures. Numerical examples have been presented in this work for air - GaN interfaces ($n = 1$ to 2.3) for the 2 - 12 μm spectral region. In fact, it is obvious that similar results could also be obtained for any other interface (such as air-GaAs and air-InP). In theory, it is almost possible to design perfect AR coatings consisting of relatively few layers and a small overall optical thickness. The problem is that, for the special and most important case when the incident medium is air, this type of a solution requires layers with refractive indices that are close to unity. For this reason the implementation of perfect AR coatings of the above type for substrate-air interfaces is much more difficult.

CHAPTER 6

CONCLUSIONS AND FUTURE POSSIBILITIES

6.1 Conclusions

Multi-band detectors have many potential applications in military, medical imaging, remote sensing, and fire/flame detection. Hence, development and improvement of these detectors in the UV and IR region is very important. Therefore, this work represents design and development of UV and IR detectors and the application of nanostructured multilayer AR coatings for improved light throughput into the detector (due to the effect of drastic reduction of reflected light) even at a high angle of incidence and a broad spectral range.

Among the different types of multi-band detectors, GaN/AlGaN based UV/IR dual-band detectors possess a significant role due to its blindness to visible light. Therefore, these results have been presented for a novel GaN/AlGaN single element detector capable of simultaneously measuring both the UV (250 - 360 nm) and IR (5 - 14 μm) responses with near zero spectral crosstalk, using three separate contacts. This has lead this detector to acquire a unique feature, where the detector has separate active regions for UV and IR radiation detection. The IR response is due to free carrier absorption in the emitters and internal photoemission over the emitter barrier interface, while the UV response is due to the interband absorption in the top AlGaN layer. Moreover, the thresholds of the UV and IR responses can be tailored by adjusting the Al fraction in the AlGaN layer.

In order to determine the feasibility of the phosphide based materials to further improve IR detectors, the mid and far-IR absorption processes have been investigated in p-type InP thin films grown on semi-insulating InP substrate. However, one of the atmospheric windows, 8 - 14 μm, is a crucial spectral region that falls into the scope of IVB effects in which the absorption coefficient and refractive index is sensitive to the doping concentration. Therefore, it emphasizes the importance of the corresponding optical constants along with their doping

dependence which will be useful for modeling semiconductor structures. To the best of my knowledge, this work provides the first experimental evidence of temperature dependence of hole effective mass in p-type InP thin films. These findings will be a crucial contribution to design of mid- and far-IR group-III Phosphide based detectors and QC lasers operating at or below room temperature.

Furthermore, the above findings on p-InP thin films have lead us to develop an IR detector based on a p-InGaAsP/InP heterostructures which demonstrate the IVB transitions of p-InGaAsP material. Therefore, the response obtained is primarily from heavy/light hole to split-off transitions. Moreover, the photovoltaic mode operation of this device will have lower dark current and hence better D*. In addition, the detector showed D^* of 2.5×10^5 Jones at 2.3 μm and 1.8×10^4 Jones at 4.5 μm for 80 K and for photovoltaic response. Furthermore, the temperature dependence of the detector response and IVB transitions are also discussed. Importantly, the split-off threshold wavelength of the detector can be varied from 3.5 - 11.2 μm by changing the As fraction of the InGaAsP emitters.

Interestingly, studies have demonstrated that the multilayer AR coatings which consist of a graded refractive index profile, can be used to obtain a very low reflectance even at the oblique angles of incidence over a broad spectral range. In theory, it is almost possible to design perfect AR coatings consisted of relatively few layers and a small overall optical thickness. Moreover, numerical examples with less number of layers have been presented in this work for air - GaN interfaces ($n = 1$ to 2.3) for the 2 - 12 μm spectral region. However, the feasibility of these AR coatings is made possible by recent developments in low-refractive index TiO_2 and SiO_2 nanostructured material. Therefore in this study, in order to better understand the effective refractive index of the single layer TiO_2 nanorod thin films, optical characterization of single layer TiO_2 nanorods grown on glass and Si substrate has been performed in the visible and IR wavelength regions.

6.2 Future Possibilities

Importantly, in addition to the present findings it is worthy to put forth some suggestions in order to improve the efficiency of the UV/IR dual-band detectors. Foremost, to further improve the IR response of the GaN/AlGaN UV/IR dual-band detector, addition of more periods of GaN/AlGaN in the IR-active region is suggested. In addition, by using AlGaN as emitters, IR threshold can be tailored without changing the UV threshold. On the otherhand, the IR threshold can be shifted to short wavelength (near-IR) to reduce the dark current and increase the operating temperature of the detector. Moreover, the barriers in the HEIWIP structure can also be modified to have a gradient which will enhance the photovoltaic operation of the device. Thus, due to this photovoltaic operation, device will require low power and have reduced low frequency noise. As reported for similar GaAs/AlGaAs HEIWIP IR detectors, these type of detectors have high D*. They exhibit no thermally assisted tunneling currents, and hence higher operating temperatures. Furthermore, IVB absorption of p-GaN can be useful to extend the IR threshold to far-IR region ($\lambda > 60\mu$m) with better performance. Another suggestion would be to implement GaN/AlGaN Quantum Well Infrared Photodetectors (QWIPs). It has been shown [45] that GaN/AlGaN QWIPs having threshold wavelengths up to 6 μm (with broad spectral peaks) which can be operated at room temperature. Moreover, the threshold wavelength can also be extended to longer wavelength with further modifications to the QWIP structure. The dark current in the UV-active region is mainly determined by thermionic emission over the work function at the top emitter/barrier interfacial work function. This dark current can be further reduced (even at high operating temperatures) by increasing this interfacial work function by increasing the Al composition in the barrier, hence leading to higher D*. However, this will shift the UV threshold into deep UV region. In addition, the UV response can be further increased by increasing the thickness of the AlGaN layer in order to absorb almost all of the UV passing through the top AlGaN layer. Furthermore, the thickness of the top contact layer can be reduced to decrease the unwanted absorption in the top n-GaN contact layer, hence allowing

more light throughput into the detector. However, this will create non-uniformity in the field. In order to overcome this issue interdigitated finger contacts can be directly deposited on top surface of the detector.[39] This will allow the generation of a lateral applied electric field. Furthermore, the absorption in the top n-GaN contact layer can be eliminated by directly depositing interdigitated contacts on the top AlGaN layer[41] as described in Section 2.6.

So far, our group has studied IVB absorption and other material parameters in p-type GaAs and InP thin films using non-destructive optical characterization techniques. It would be interesting to extend this investigation into p-GaN thin films in order to study the IVB absorption in far-IR region. These studies will be useful for designing IR detectors based on IVB transitions in far-IR. However, these measurements should be carried out in cryogenic temperatures since the split-off energy of GaN is less than 20 meV.

The responsivity of the InGaAsP/InP detector can be further improved by increasing the number of emitter/barrier periods. For an instance, the responsivity can be increased by a factor of 3 by increasing the number of periods from 10 to 30. This will also increase the device impedance leading to a much stable operation. In addition, if future growth can achieve higher doping for p-InGaAsP then we do not need to implement InGaAs layers as the top and bottom contacts. The photovoltaic response of this detector could be due to a slight gradient in the barriers which occurred from growth process. However, the barriers can be intentionally graded to enhance this photovoltaic response. Because, similar GaAs/AlGaAs photovoltaic detectors [43] have shown that the response can be optimized by using a graded-barriers that reduces trapping and increases the gain. In addition, we can test the split-off threshold wavelength variation by having additional detectors with different As alloy fractions. Thus, this work suggests that the materials other than InGaAsP may help to extend the coverage to longer wavelengths by using materials such as GaN that may be able to operate with threshold wavelengths 60 μm or beyond at elevated temperatures.

In addition, I have also shown the optical characterization of single layer TiO_2 nanorod layers grown at different vapor flux angles. Interestingly, this study can be further expanded

to characterize more samples having different vapor flux angles which will lead to better understand the refractive index variation with vapor flux angle. Therefore, a study with suggested improvements will be beneficial for the growers to fine tune the refractive index of the nanorod layers required for the multi-layer AR coatings. In addition, optical characterization of multi-layer nanorods is important to understand the partial reflection at each interface and the over all total reflection. In designing optimized multi-layer AR coatings, it is obvious that similar results could also be obtained for any other interface (such as air-GaAs and air-InP). However, one of the problems that will be encountered is that, for the special and most important case when the incident medium is air, this type of a solution requires layers with refractive indices that are close to unity. For this reason the implementation of perfect AR coatings of the above type for substrate-air interfaces is much more difficult. Therefore it is worthy to spend more time on characterizing AR coatings. On the other hand, these low-refractive nanorod layers would be highly desirable for many other applications, such as distributed Bragg reflectors,[99, 100] omnidirectional reflectors,[101, 102] optical interconnects,[103] optical microresonators,[104] and light-emitting diodes.[105].

In conclusion, with these further suggestions it can be anticipated that the future studies would enhance the quality of UV and IR detectors, AR coatings, and material characterization of group III-V semiconductor thin films.

REFERENCES

[1] C. H. Henry, R. A. Logan, F. R. Merritt, and J. P. Luongo, IEEE J. Quantum Electron. **19**, 947 (1983).

[2] D. Schneider, Z. Phys. B **100**, 33 (1996).

[3] Y. P. Varshni, Physica (Amsterdam) **34**, 149 (1967).

[4] L. Pavesi, F. Piazza, A. Rudra, J. F. Carlin, and M. Ilegems, Phy. Rev. B **44**, 9052 (1991).

[5] D. Starikov, C. Boney, R. Pillai, and A. Bensaoula, Dual-band uv/ir optical sensors for fire and flame detection and target recognition, in *Proceedings of the ISA/IEEE Sensors for Industry Conference (IEEE, 2004)*, pages 36–40, 2004.

[6] D. H. Huang, Proc. of the Space Sensing and Situtational Awareness Meeting of NATO Specialists (2006).

[7] D. B. Law, SPIE Proceedings **2938**, 288 (1997).

[8] M. A. Khan, J. N. Kuznia, D. T. Olson, M. Blasingame, and A. R. Bhattarai, Appl. Phys. Lett. **63**, 2455 (1993).

[9] D. Walker, X. Zhang, P. Kung, A. Saxler, S. Javadpour, J. Xu, and M. Razeghi, Appl. Phys. Lett. **68**, 2100 (1996).

[10] Y. Lao and A. G. U. Perera, J. App. Phys. **109**, 103528 (2011).

[11] A. G. U. Perera, H. X. Yuan, and M. H. Francombe, J. Appl. Phys. **77**, 915 (1995).

[12] D. G. Esaev, M. B. M. Rinzan, S. G. Matsik, A. G. U. Perera, H. C. Liu, B. N. Zvonkov, V. I. Gavrilenko, and A. A. Belyanin, J. Appl. Phys. **95**, 512 (2004).

[13] S. G. Matsik, M. B. M. Rinzan, A. G. U. Perera, H. C. Liu, Z. R. Wasilewski, and M. Buchanan, Appl. Phys. Lett. **82**, 139 (2003).

[14] A. G. U. Perera, S. G. Matsik, B. Yaldiz, H. C. Liu, A. Shen, M. Gao, Z. R. Wasilewski, and M. Buchanan, Appl. Phys. Lett. **78**, 2241 (2001).

[15] G. Ariyawansa, M. B. M. Rinzan, M. Alevli, M. Strassburg, N. Dietz, A. G. U. Perera, S. G. Matsik, A. Asghar, I. T. Ferguson, H. Luo, A. Bezinger, and H. C. Liu, Appl. Phys. Lett. **89**, 091113 (2006).

[16] D. G. Esaev, M. B. M. Rinzan, S. G. Matsik, and A. G. U. Perera, J. Appl. Phys. **96**, 4588 (2004).

[17] J.-Q. Xi, M. F. Schubert, J. K. Kim, E. F. Schubert, S.-Y. Chen, M. Lin, W. Liu, and J. A. Smart, Nature Photonics **1**, 176 (2007).

[18] S. Forrest, P. Schmidt, R. Wilson, and M. Kaplan, Appl. Phys. Lett. **45**, 1199 (1984).

[19] T. Fukunaga, M. Wada, H. Asano, and T. Hayakawa, J. Appl. Phys **34**, L1175 (1995).

[20] A. G. U. Perera, S. G. Matsik, P. V. V. Jayaweera, K. Tennakone, H. C. Liu, M. Buchanan, G. Von Winckel, A. Stintz, and S. Krishna, Appl. Phys. Lett. **89**, 131118 (2006).

[21] G. Ariyawansa, P. V. V. Jayaweera, A. G. U. Perera, S. G. Matsik, M. Buchanan, Z. R. Wasilewski, and H. C. Liu, Opt. Lett. **34**, 2036 (2009).

[22] G. Ariyawansa, Y. Aytac, A. G. U. Perera, S. G. Matsik, M. Buchanan, Z. R. Wasilewski, and H. C. Liu, Appl. Phys. Lett. **97**, 231102 (2010).

[23] Y.-F. Lao, G. Ariyawansa, and A. G. U. Perera, **110**, 043112 (2011).

[24] G. Ariyawansa, M. B. M. Rinzan, D. G. Esaev, S. G. Matsik, G. Hastings, A. G. U. Perera, H. C. Liu, B. N. Zvonkov, and V. I. Gavrilenko, Appl. Phy. Lett. **86**, 143510 (2005).

[25] A. Goldberg, P. N. Uppal, and M. Winn, Infrared Phys. Technol. **44**, 427 (2003).

[26] H. C. Liu, C. Y. Song, A. Shen, M. Gao, Z. R. Wasilewski, and M. Buchanan, Appl. Phys. Lett. **77**, 2437 (2000).

[27] M. P. Touse, G. Karunasiri, K. R. Lantz, H. Li, and T. Mei, Appl. Phys. Lett. **86**, 093501 (2005).

[28] T. Fujii, Y. Gao, R. Sharma, E. L. Hu, S. P. DenBaars, and S. Nakamura, Applied Physics Letters **84**, 855 (2004).

[29] J. Han, M. H. Crawford, R. J. Shul, J. J. Figiel, M. Banas, L. Zhang, Y. K. Song, H. Zhou, and A. V. Nurmikko, Applied Physics Letters **73**, 1688 (1998).

[30] K. Kojima, U. T. Schwarz, M. Funato, Y. Kawakami, S. Nagahama, and T. Mukai, Opt. Express **15**, 7730 (2007).

[31] R. C. Jayasinghe, G. Ariyawansa, N. Dietz, A. G. U. Perera, S. G. Matsik, H. B. Yu, I. T. Ferguson, A. Bezinger, S. R. Laframboise, M. Buchanan, and H. C. Liu, Opt. Lett. **33**, 2422 (2008).

[32] O. Katz, V. Garber, B. Meyler, G. Bahir, and J. Salzman, Appl. Phys. Lett. **80**, 347 (2002).

[33] S. K. Zhang, W. B. Wang, I. Shtau, F. Yun, L. He, H. Morkoc, X. Zhou, M. Tamargo, and R. R. Alfano, Applied Physics Letters **81**, 4862 (2002).

[34] V. Adivarahan, G. Simin, J. W. Yang, A. Lunev, M. Asif, Khan, N. Pala, M. Shur, and R. Gaska, Appl. Phys. Lett. **77**, 863 (2000).

[35] J. Z. Li, J. Y. Lin, H. X. Jiang, and M. A. Khan, Appl. Phys. Lett. **72**, 2868 (1998).

[36] W. Shen, A. Perera, H. Liu, M. Buchanan, and W. Schaff, Appl. Phys. Lett. **71**, 2677 (1997).

[37] H. Jiang, G. Y. Zhao, H. Ishikawa, T. Egawa, T. Jimbo, and M. Umeno, J. App. Phys. **89**, 1046 (2001).

[38] L. Chernyak, A. Osinsky, and A. Schultea, Solid-State Electron. **45**, 1687 (2001).

[39] H. Kim, S.-J. Park, H. Hwang, and N.-M. Park, Appl. Phys. Lett. **81**, 1326 (2002).

[40] O. Jani, I. Ferguson, C. Honsberg, and S. Kurtz, Appl. Phys. Lett. **91**, 132117 (2007).

[41] J. Li, M. Zhao, and X. F. Wang, Physica B: Condensed Matter **405**, 996 (2010).

[42] J. M. V. Hove, R. Hickman, J. J. Klaassen, P. P. Chow, and P. P. Ruden, Appl. Phys. Lett. **70**, 2282 (1997).

[43] P. K. D. D. P. Pitigala, S. G. Matsik, A. G. U. Perera, S. P. Khanna, L. H. Li, E. H. Linfield, Z. R. W. M. Buchanan, and H. C. Liu, J. Appl. Phys. **111**, 084505 (2012).

[44] P. V. V. Jayaweera, S. G. Matsik, A. G. U. Perera, H. C. Liu, M. Buchanan, and Z. R. Wasilewski, Appl. Phys. Lett. **93**, 21105 (2008).

[45] B. Sherliker, M. Halsall, I. Kasalynas, D. Seliuta, G. Valusis, M. Vengris, M. Barkauskas, V. Sirutkaitis, P. Harrison, V. D. Jovanovic, D. Indjin, Z. Ikonic, P. J. Parbrook, T. Wang, and P. D. Buckle, Semicond. Sci. Technol. **22**, 1240 (2007).

[46] M. Klein and T. Furtac, *Optics*, Wiley, New York, 1986.

[47] C. C. Katsidis and D. I. Siapkas, Appl. Optics **41**, 3978 (2002).

[48] D. K. Sengupta, S. L. Jackson, D. Ahmari, H. C. Kuo, J. I. Malin, S. Thomas, M. Feng, G. E. Stillman, Y. C. Chang, L. Li, and H. C. Liu, Appl. Phys. Lett. **69**, 3209 (1996).

[49] Y. F. Lao, P. K. D. D. P. Pitigala, A. G. U. Perera, H. C. Liu, M. Buchanan, Z. R. Wasilewski, K. K. Choi, and P. Wijewarnasuriya, Appl. Phys. Lett. **97**, 091104 (2010).

[50] I. Vurgaftman, J. R. Meyer, and L. R. Ram-Mohan, J. Appl. Phys. **89**, 5815 (2001).

[51] R. C. Jayasinghe, Y. F. Lao, A. G. U. Perera, M. Hammar, C. F. Cao, and H. Z. Wu, J. Phys.: Condens. Matter (submitted) (2012).

[52] D. P. Bour and S. W. Corzine, in *US Patent; Vol. US 2006/0203865 Al*, 2006.

[53] E. S. Koteles and W. R. Datars, Solid State Commun. **19**, 221 (1976).

[54] B. Ulrici and E. Jahne, Physica Status Solidi (b) **74**, 601 (1976).

[55] S. Kakimoto and H. Watanabe, J. Appl. Phys. **85**, 1822 (1999).

[56] Z. G. Hu, M. Strassburg, N. Dietz, A. G. U. Perera, A. Asghar, and I. T. Ferguson, Phys. Rev. B **72**, 245326 (2005).

[57] Z. G. Hu, A. B. Weerasekara, N. Dietz, A. G. U. Perera, M. Strassburg, M. H. Kane, A. Asghar, and I. T. Ferguson, Phys. Rev. B **75**, 205320 (2007).

[58] S. Adachi, *GaAs and related materials*, World Scientific, Singapore, 1994.

[59] J. S. Blakemore, J. Appl. Phys. **53**, R123 (1982).

[60] M. B. M. Rinzan, D. G. Esaev, A. G. U. Perera, S. G. Matsik, G. von Winckel, A. Stintz, and S. Krishna, Appl. Phys. Lett. **85**, 5236 (2004).

[61] D. N. Talwar, Appl. Phy. Lett. **97**, 051902 (2010).

[62] T. W. Noh, P. H. Song, S.-I. Lee, D. C. Harris, J. R. Gaines, and J. C. Garland, Phys. Rev. B **46**, 4212 (1992).

[63] Y. C. A. Djurisic and E. H. Li, Materials Science and Engineering R **38**, 237 (2002).

[64] W. Songprakob, R. Zallen, W. K. Liu, and K. L. Bacher, Phys. Rev. B **62**, 4501 (2000).

[65] W. Press, B. Flannery, S. Teukolsky, and W. Vetterling, *Numerical Recipes*, Cambridge University Press, Cambridge, 1986.

[66] W. Songprakob, R. Zallen, D. V. Tsu, and W. K. Liu, J. Appl. Phys. **91**, 171 (2002).

[67] P. Y. Yu and M. Cardona, *Fundamentals of Semiconductors: Physics and Materials Properties*, Springer-Verlag Berlin Heidelberg, 2005.

[68] E. Kioupakis, P. Rinke, A. Schleife, F. Bechstedt, and C. G. V. d. Walle, Phy. Rev. B **81**, 241201(R) (2010).

[69] G. Irmer, M. Wenzel, and J. Monecke, Phys. Status Solidi B **195**, 85 (1996).

[70] K. Hansen, E. Peiner, A. Schlachetzki, and M. V. Ortenberg, J. Electron. Mater **23**, 935 (1994).

[71] M. Osinski, Second international conference on indium phosphide and related materials, in *Heavy-hole effective mass in InP-a critical examination*, pages 330–333, 1990.

[72] S. Adachi, *Properties of group-IV, III-V and II-VI semiconductors*, John Wiley & Sons, Ltd, West Sussex, 2005.

[73] Z. Hang, Solid State Commun. **73**, 15 (1990).

[74] M. Bass, *Handbook of Optics*, volume 2, McGraw Hill, 2nd edition, 1995.

[75] M. S. Whalen, J. Appl. Phys. **53**, 4340 (1982).

[76] P. Martin, E. M. Skouri, L. Chusseau, C. Alibert, and H. Bissessur, Appl. Phy. Lett. **67**, 881 (1995).

[77] S. G. Matsik, P. V. V. Jayaweera, A. G. U. Perera, K. K. Choi, and P. Wijewarnasuriya, J. Appl. Phys. **106**, 1064503 (2009).

[78] O. O. Cellek, S. Ozer, and C. Besikci, IEEE J. Quantum Electron. **41**, 980 (2005).

[79] S. D. Gunapala, B. F. Levine, D. Ritter, R. A. Hamm, and M. B. Panish, Appl. Phys. Lett. **60**, 636 (1992).

[80] S. G. Matsik, M. B. M. Rinzan, D. G. Esaev, A. G. U. Perera, H. C. Liu, and M. Buchanan, Appl. Phys. Lett. **84**, 3435 (2004).

[81] Y. F. Lao, P. V. V. Jayaweera, S. G. Matsik, A. G. U. Perera, H. C. Liu, M. Buchanan, and Z. R. Wasilewski, IEEE Transactions on Electron Devices **57**, 1230 (2010).

[82] M. S. Shishodia and A. G. U. Perera, J. Appl. Phys. **109**, 043108 (2011).

[83] M. S. Shishodia, P. V. V. Jayaweera, S. G. Matsik, A. G. U. Perera, H. C. Liu, and M. Buchanan, Photonics Nanostruct. Fundam. Appl. **9(1)**, 95 (2011).

[84] R. C. Jayasinghe, A. G. U. Perera, H. Zhu, and Y. Zhao, Optics Lett. (Submitted) .

[85] Y. P. He, Z. Y. Zhang, and Y. P. Zhao, J. Vac. Sci. Tech. B **26(4)**, 1350 (2008).

[86] G. K. Larsen, R. Fitzmorris, J. Z. Zhang, and Y. Zhao, J. Phys. Chem. C **115**, 16892 (2011).

[87] N. Xu, Z. Shi, Y. Fan, J. Dong, J. Shi, and M. Hu, Ind. Eng. Chem. Res. **38**, 373 (1999).

[88] M. Kennedy, F. Kruis, H. Fissan, B. Mehta, and G. Dumpich, J. Appl. Phys. **93**, 551 (2003).

[89] B. Richards, J. Cotter, and S. Wenham, in *Proceedings of the 28th IEEE PVSC (IEEE)*, page 375, 2000.

[90] M. Born and E. Wolf, *Principles of Optics: Electromagnetic Theory of Propagation, Interference and Diffraction of Light*, Cambridge University Press, 7th edition, 1999.

[91] V. Kranenburg and C. Lodder, Mater. Sci. Eng. **R 11**, 295 (1994).

[92] D. Brian and B. Michael, Encyclopedia Nanosci. Nanotechnol. **6**, 703 (2004).

[93] R. Messier, V. Venugopal, and P. Sunal, J. Vac. Sci. Technol. A **18**, 1538 (2000).

[94] M. Bass, C. DeCusatis, J. Enoch, G. Li, V. N. Mahajan, V. Lakshminarayanan, E. V. Stryland, and C. MacDonald, *Handbook of Optics*, McGraw-Hill, 3rd edition, 2009.

[95] W. H. Southwell, Opt. Lett. **8(11)**, 584 (1983).

[96] N. semiconductor materials, in *Characteristics and Properties.*, Available at http://www.ioffe.ru/SVA/NSM/.

[97] S. Martin, J. Rivory, and M. Schoenauer, Appl. Opt. **34(13)**, 2247 (1995).

[98] M. F. Schubert, F. W. Mont, S. Chhajed, D. J. Poxson, J. K. Kim, and E. F. Schubert, Opt. Express **16(8)**, 5290 (2008).

[99] R. Sharma, E. D. Haberer, C. Meier, E. L. Hu, and S. Nakamura, Appl. Phys. Lett. **87**, 051107 (2005).

[100] S.-T. Ho, S. L. McCall, R. E. Slusher, L. N. Pfeiffer, K. W. West, A. F. J. Levi, G. E. Blonder, and J. L. Jewell, Appl. Phys. Lett. **57**, 1387 (1990).

[101] J.-Q. Xi, M. Ojha, J. L. Plawsky, W. N. Gill, J. K. Kim, , and E. F. Schubert, Appl. Phys. Lett. **87**, 031111 (2005).

[102] J.-Q. Xi, M. Ojha, W. Cho, J. L. Plawsky, W. N. Gill, T. Gessmann, and E. F. Schubert, Opt. Lett. **30**, 1518 (2005).

[103] A. Jain, S. Rogojevic, S. Ponoth, N. Agarwal, I. Matthew, W. Gill, P. Persans, M. Tomozawa, J. Plawsky, and E. Simonyi, Solid Thin Films **398-399**, 513 (2001).

[104] Q. Xu, V. R. Almeida, R. R. Panepucci, and M. Lipson, Opt. Lett. **29**, 1626 (2004).

[105] J. K. Kim, T. Gessmann, E. F. Schubert, J.-Q. Xi, H. Luo, J. Cho, C. Sone, and Y. Park, Appl. Phys. Lett. **88**, 013501 (2006).

Appendix A

Device Characterization

A.1 Spectral Responsivity

Spectral responsivity is the output current per Watt of incident power when noise is not considered.

$$R = \frac{S}{PA} \tag{A.1}$$

where S is the signal output in Amperes, P is the incident light intensity in W/cm^2 and A is the detector active area in cm^2.

A.2 Quantum efficiency

The photocurrent of the detector for given wavelength λ can be expressed as

$$I_{sc} = \frac{\eta q g P A \lambda}{hc} \tag{A.2}$$

where λ is the wavelength, h is Planck's constant, c is the speed of light and q is the electron charge. The quantum efficiency η is the number of electron hole pairs generated per incident photon. The gain g is the number of carriers collected at the contact per generated carrier.

Therefore, the current responsivity can be given as

$$R_I(\lambda) = \frac{I_{SC}}{PA} = \frac{\eta q g \lambda}{hc} = \frac{\eta g \lambda}{1.24} \tag{A.3}$$

Here λ should be in μm and R_I in A/W. Then, the quantum efficiency η is given by

$$R_I(\lambda) = 1.24 \frac{R_I(\lambda)}{\lambda g} \times 100\% \tag{A.4}$$

A.3 Noise Equivalent Power

Noise Equivalent Power (NEP) is the incident light power needed to produce an output signal equal to the intrinsic noise level of the detector.

$$NEP = \frac{PA}{S/N\sqrt{\Delta f}} \tag{A.5}$$

A.4 Specific Detectivity

The specific detectivity is equal to the reciprocal of noise equivalent power, normalized to unit area and unit bandwidth and is given by

$$D^* = \frac{S/N\sqrt{\Delta f}}{P\sqrt{A}} = \frac{\sqrt{A}}{NEP} = \frac{R_I\sqrt{A}}{N/\sqrt{\Delta f}} \tag{A.6}$$

The noise output (N) is found in terms of noise current density (N_d)

$$N_d = \frac{N^2}{\Delta f} \tag{A.7}$$

Thus Eq. A.6 can be deduced as follows

$$D^* = \frac{R_I.\sqrt{A}}{\sqrt{N_d}} \tag{A.8}$$

Here the units of D^* are cm$\sqrt{Hz}/W$ or Jones. The D^* of a device at different temperatures and applied biases is obtained from the measured R_I, N_d, and the illuminated area of the detector (A). A dual channel Fast Fourier Transform (FFT) signal analyzer and a SR570 low noise current pre-amplifier are used to measure N_d. A thick copper plate at the device temperature is used as the radiation block to provide the dark conditions for the measurements.

Appendix B

Programs Developed with LabView: UV/IR Dual-Band Spectrometer with Single Optical Chopper

The dual-band spectrometer is controlled using an in house software program developed with LabVIEW 7.1. The main front panel and its functions are explained in following figures. The setup is a combination of UV and IR spectrometers. The UV and IR components are controlled simultaneously. Also the UV and IR response curves are visualized in two panels. There are two scanning modes that user has to select: (i) detector response with changing wavelength, and (ii) detector response with time. In general, when one component of the response is scanned over the wavelength, the other component is scanned over the time. Before starting the scan, all the parameters have to be set properly. Although only two major panels are shown in this section, there are a number of sub-VIs (virtual-interfaces) and popup windows, which provide sufficient instructions during the runtime, linked with the main front panel.

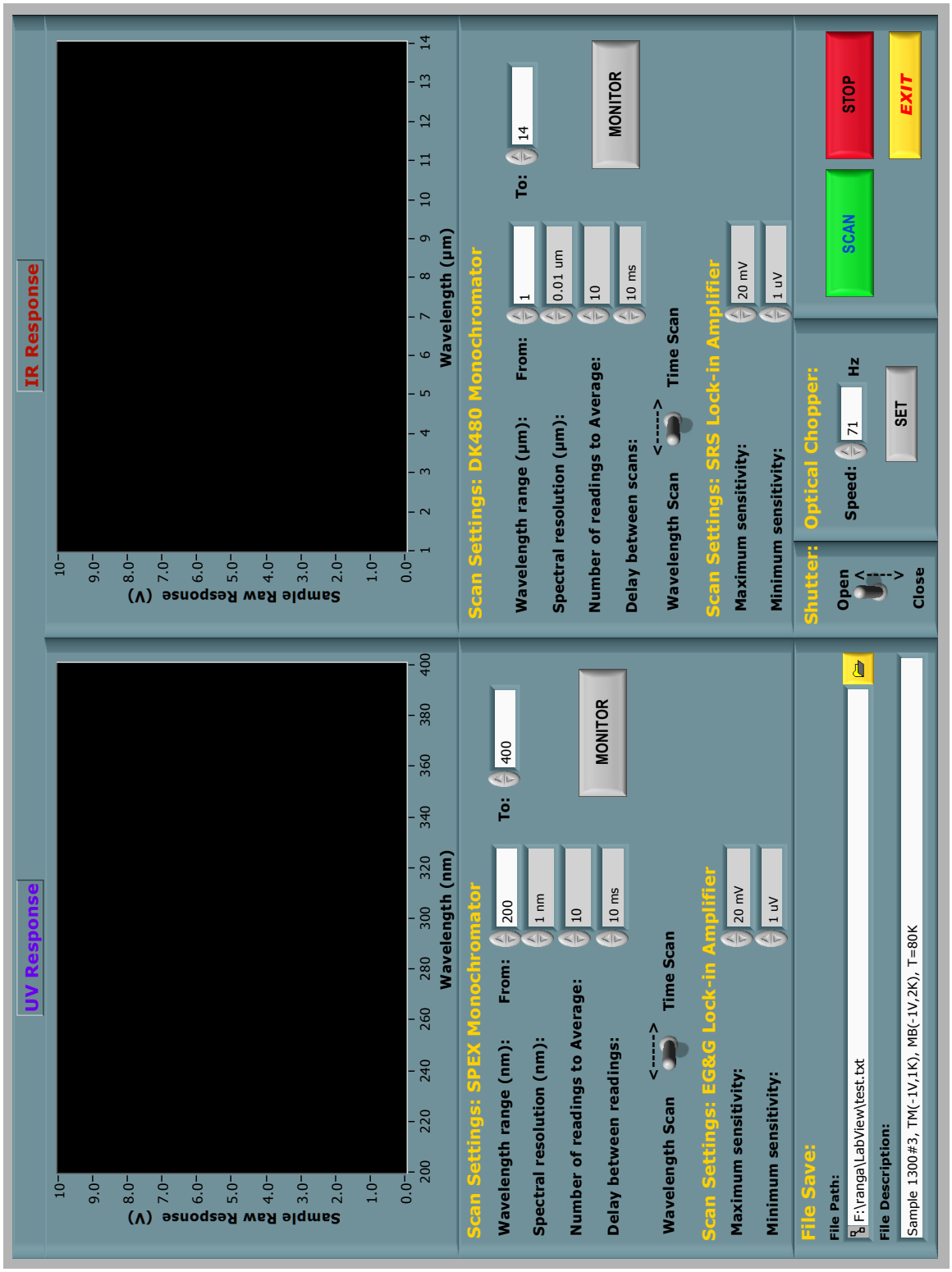

Figure B.1 The main front panel of the UV/IR dual-band spectrometer software. The user can observe the real time raw spectra from both UV- and IR-active regions of the UV/IR dual-band detector.

Appendix C

Programs Developed with MATLAB

C.1 Transfer-matrix Method

This program was rewritten in MATLAB Version 7.14.

```
%%%%%%%% Anti-reflcection coating calculatiions with TMM %%%%%%%%%%%%%
clear all
clc
%Define constants
eps0=8.85418782e-12; % Dielectric constant of vacuum (units=F/m)
k=1.380662e-23; % Boltsman constant(units=J/K)
q=1.6021892e-19; % Electron charge (units= C)
h=6.626176e-34; % Plank constant (Units=J/Hz)
m0=9.109534e-31; % Electron mass (Units=kg)
mu0=1.256637e-6; % (Unitis =H/m)
c=2.998e8; % Speed of light (Unitis= m/s)
%%%%%%%%%%%%%%%%%%

n=[1.0 1.08 1.26  1.51 1.7 2.01];
ns=2.3;
%D=[0 0.3e-6 0.3e-6 0.3e-6 0.3e-6 0.3e-6 0.3e-6 0.3e-6 0.3e-6
0.3e-6 0.3e-6 0.3e-6 0.3e-6 0.3e-6 0.3e-6 0.3e-6];
%t=0.1e-6;
D=[0 0.53e-6 0.46e-6 0.35e-6 0.2e-6 0.25e-6];
Ds= 450e-6; % Substrate thickness
```

```
theta_v=pi()/180*70; % Incident angle in vaccum medium
nv=1;

l_Max=numel(n)-1;

MaxPts=200;
LowerWN=500;
UpperWN=6000;

for z=1:MaxPts
wn=LowerWN+((UpperWN-LowerWN)/(MaxPts-1)*z);
Wm=2*pi()*c*wn*100; % cm-1 units for wavenumber
kw=Wm/c;

TTs=[1 0;0 1];
TTp=[1 0;0 1];
theta_l=theta_v;

for l=1:l_Max
theta_2=theta_new(n(l),theta_l,n(l+1));
Ts=TS(n(l),theta_l,n(l+1),theta_2);
Tp=TP(n(l),theta_l,n(l+1),theta_2);
P=Prop(n(l+1),theta_2,D(l+1),kw);
TTs=TTs*(Ts*P);
TTp=TTp*Tp*P;
theta_l=theta_2;
MaxLyr=l+1;
end
```

```
%ns=EpsiLayer(epsi_high,plasma_f,plasma_broad,TO_f,TO_s,TO_broad,wm);
theta_s=theta_new(n(MaxLyr),theta_l,ns);
Tss=TS(n(MaxLyr),theta_l,ns,theta_s);
Tsp=TP(n(MaxLyr),theta_l,ns,theta_s);
TTs=TTs*Tss;
TTp=TTp*Tsp;

X(z)=10000/wn; %convert to wavelength (microns)
Xwn(z)=wn;
RRS(z)=abs(TTs(2,1)/TTs(1,1))^2;
RRP(z)=abs(TTp(2,1)/TTp(1,1))^2;
RRavg(z)=(RRS(z)+RRP(z))/2;
end

plot(Xwn,RRavg)
%dlmwrite('data.txt', RR,'delimiter', '\t', 'precision', 6)

R = [X; RRS; RRP; RRavg];
fileID = fopen('MatlabCalR.txt','w');
%fprintf(fileID,'%6s %12s\n','wn','R');
fprintf(fileID,'%12.8f\t %12.8f\t %12.8f\t %12.8f\n',R);
fclose(fileID);

N = [D; n];
fileID = fopen('RefIndex.txt','w');
fprintf(fileID,'%20.20f\t %12.8f\n',N);
fclose(fileID);
```